þÿ A cholesterol analog stabilizes the human ²2-ad receptor nonlinearly with temperature

Serdiuk, Tetiana

2022-06-07

Serdiuk , T , Manna , M , Zhang , C , Mari , S A , Kulig , W , Pluhackova , K , Kobilka , B K , Vattulainen , I & Müller , D J 2022 , ' A cholesterol analog stabilizes the human þÿ²2-adrenergic receptor nonlinearly with temperature ' , Science signali 7031 . https://doi.org/10.1126/scisignal.abi7031

http://hdl.handle.net/10138/352223
https://doi.org/10.1126/scisignal.abi7031

unspecified
acceptedVersion

A cholesterol analog stabilizes the human β_2-adrenergic receptor nonlinearly with temperature

Tetiana Serdiuk[1,2], Moutusi Manna[3], Cheng Zhang[4,5], Stefania A. Mari[1], Waldemar Kulig[6], Kristyna Pluhackova[1], Brian K. Kobilka[4], Ilpo Vattulainen[6,7], Daniel J. Müller[1]*

[1]Department of Biosystems Science and Engineering, ETH Zurich, CH-4058 Basel, Switzerland. [2]Institute of Molecular Systems Biology, Department of Biology, ETH Zurich, CH-8093 Zurich, Switzerland. [3]Applied Phycology and Biotechnology Division, CSIR–Central Salt and Marine Chemicals Research Institute, Bhavnagar–364002, Gujarat, India. [4]Department of Cellular Physiology and Medicine, Stanford University School of Medicine, Palo Alto, CA 94305, USA. [5]Department of Pharmacology and Chemical Biology, School of Medicine, University of Pittsburgh, Pittsburgh, PA 15261, USA. [6]Department of Physics, University of Helsinki, P. O. Box 64, FI-00014 Helsinki, Finland. [7]Computational Physics Laboratory, Tampere University, P. O. Box 692, FI-33014, Tampere, Finland.

*Corresponding author. Email: daniel.mueller@bsse.ethz.ch

ABSTRACT

In cell membranes, G protein–coupled receptors (GPCRs) mingle with cholesterol, which modulates their assembly, stability, and conformation. Previous studies have shown how cholesterol modulates the structural properties of GPCRs at ambient temperature. Here, we characterized the mechanical, kinetic, and energetic properties of the human β_2-adrenergic receptor (β_2AR) in the presence and absence of the cholesterol analog cholesteryl hemisuccinate (CHS) at room temperature (25°C), physiological temperature (37°C), and human hyperthermia (42°C). We found that CHS stabilized various structural regions of β_2AR differentially, which changed nonlinearly with temperature. Thereby, the strongest effects were observed for structural regions that are important for receptor signaling. Moreover, at 37°C, but not at 25°C or 42°C, CHS caused the β_2AR to increase and stabilize conformational sub-states to adopt to basal activity. These findings indicate that the nonlinear, temperature-dependent action of CHS in modulating the structural properties of this GPCR is optimized for 37°C.

INTRODUCTION

G protein–coupled receptors (GPCRs) constitute one of the largest families of human transmembrane proteins (*1, 2*) that sense extracellular signals and transduce this information into the cell to initiate cellular responses (*3, 4*). Members of the GPCR family modulate responses to hormones and neurotransmitters, and play crucial roles in vision, smell, taste, the immune response, and inflammation. One of the structurally and functionally best studied GPCRs is the human β_2-adrenergic receptor (β_2AR), which serves as a model of the largest class, class A, of the GPCR family (*5, 6*). Because β_2AR binds to adrenaline in bronchial tissue, promoting smooth muscle relaxation, and to noradrenaline in cardiac tissues, playing a role in heart function and failure, it is a promising therapeutic target(*7-9*). The β_2AR and other GPCRs co-exist in multiple conformational states of which certain states become more prominent depending on the GPCR assembly, membrane lipid composition, and ligand-binding (*10-13*). Detailed insight into how GPCRs interact with the membrane environment has been provided by structural models obtained by X-ray crystallography, nuclear magnetic resonance (NMR), cryo-electron microscopy (cryo-EM), native mass spectrometry (MS), and molecular dynamics (MD) simulations (*5, 6, 12-19*). Based on this progress, we are now starting to understand how the lipid composition of the cellular membrane modulates the functional state of GPCRs (*17, 20, 21*). Among the lipids of the cell membrane, cholesterol has prominent roles in modulating the functional state and stability of GPCRs (*5, 22*). However, how and to which extent cholesterol affects the conformational stability of GPCRs remains a topic of investigation.

Cholesterol, a major component of mammalian plasma membranes, ranges in physiological concentration from 10 to 45 mol% depending on the cell type (*23-25*) and has crucial roles in

modulating the structure-function relationship of transmembrane proteins (*22, 26*). For example, cholesterol and its more water-soluble analog cholesteryl hemisuccinate (CHS) modulate the ligand-binding and functional states of GPCRs in an allosteric manner and increase the stability of GPCRs (*27-29*). On the other hand, the structure and function of GPCRs are often characterized at nonphysiological temperatures, although the temperature-dependencies of membrane receptor assembly, stability, and function have been observed frequently (*27, 30*). Thus, which of the structural properties of GPCRs are modulated by cholesterol and CHS, and how this modulation depends on the physiologically relevant temperature remain to be understood.

High-resolution structures of several GPCRs have revealed cholesterol bound to the receptors (*5, 27, 31, 32*). X-ray structures of β_2AR show cholesterol-binding sites between transmembrane α-helices TMH1, TMH2, TMH3, and TMH4 (*5, 27*). Structures of close family members of β_2AR show cholesterol- or CHS-binding sites between TMH2 and TMH4 and between TMH3and TMH5 for the β_1-adrenergic receptor (β_1AR), and between TMH2 and TMH3 and between TMH5 and TMH6 for the adenosine A2a receptor (A_{2a}AR) (*33, 34*). Complementary to such static structural models, MD simulations of the β_2AR embedded in lipid membranes support the idea that cholesterol preferentially occupies specific interaction sites of the receptor (*35-37*). Full-atomistic MD simulations spanning time ranges of up to ~100 μs show several high-affinity cholesterol-binding sites of which one is located in a cleft formed at the intracellular surface of TMH1 to TMH4, another at a cleft between TMH5 and TMH6 at the intracellular side, and two closely spaced cholesterol hot spots are located at the extracellular region of TMH5-TMH6-E3-TMH7 (*36*). Although structural models and MD simulations can unveil static and transient interactions of β_2AR and cholesterol, they cannot be used to quantify whether and to what extent cholesterol modulates the

mechanical, kinetic, and energetic properties of the receptor in physiologically relevant time ranges.

Atomic force microscopy (AFM)–based single-molecule force spectroscopy (SMFS) has been introduced to characterize the structural folding and properties of transmembrane proteins, including transporters, ion channels, and GPCRs (*38*-*42*). When applied to the human β_2AR in the presence of CHS at room temperature (*29*), dynamic SMFS (DFS) has revealed the changes that occur to the mechanical, kinetic, and energetic properties of the β_2AR upon ligand-binding (*38*). However, the understanding of how sensitive such structural properties of GPCRs are to physiological temperature ranges is limited. Here, we applied DFS experiments and atomistic MD simulations to study the role of CHS in modulating the mechanical, kinetic, and energetic properties of β_2AR at room temperature (25°C), at physiological temperature (37°C), and at temperature corresponding to hyperthermia (42°C), which leads to cellular damages in humans (*43, 44*). The insights gained, which defined the structural regions of the β_2AR that are affected by CHS and quantified how their properties depend on temperature, highlight the mechanisms by which sterols optimize the structure-function relationship of the β_2AR to physiological temperature.

RESULTS

Mapping the mechanical stability of human β_2AR

To characterize how temperature variations within the physiological range influence the mechanical stability of β_2AR, we reconstituted human β_2AR in 1,2-dioleoyl-sn-glycero-3-phosphocholine (DOPC) liposomes without or with CHS (DOPC:CHS ratio 10:1 vol:vol) (fig. S1A). The proteoliposomes were adsorbed in buffer to carbon grids or mica for ~ 1 h and imaged by transmission

electron microscopy (TEM) or AFM, respectively, where they opened-up as single-layered membrane patches (fig. S1, B to F). To characterize whether the appearance of the membranes changed with temperature, we imaged the samples at 25°C, 37°C, and 42°C by AFM (fig. S2). The membranes and β_2AR assemblies protruding from the membrane did not change appearance, thus indicating that the lipids did not undergo phase separations and that the β_2ARs did not change their assembly. After imaging the opened-up proteoliposomes by AFM in buffer at room temperature (25°C), the stylus of the AFM cantilever was pushed onto the β_2AR embedded in a DOPC membrane at ~ 700 pN for 0.5 s (Fig. 1A). In ~ 0.1% of all cases (n > 1,000,000), the mechanical contact promoted the nonspecific attachment of the N-terminal end of β_2AR to the AFM stylus (*29, 38, 45*). Subsequently, the AFM cantilever was retracted from the membrane at constant speed. During retraction, the N-terminal end of the receptor was mechanically stretched and the extraction and unfolding of a single β_2AR was recorded with a force-distance curve (Fig. 1B). As previously reported (*29, 38*), the force-distance curve showed force peaks extending to distances of ~ 80 nm, which corresponds to the contour length of the fully unfolded and stretched β_2AR polypeptide. The superimposition of 100 force-distance curves, each recorded upon mechanically unfolding a single β_2AR, revealed the common unfolding pattern of human β_2AR with eight dominant force peaks (Fig. 1C). Every force peak of the force-distance curve was fitted by the worm-like chain (WLC) model to estimate the contour length of the stepwise unfolded and stretched β_2AR polypeptide (*45*). The contour lengths of the eight force peaks were then used to localize the beginning and the end of the eight structural segments (S1 to S8) unfolded by β_2AR (Fig. 1D). The mechanical stability of each structural segment, which is typically composed of α-helices and polypeptide loops (*29, 38*), is described by the magnitude of the respective force peak (*45*).

CHS protects the β_2AR from destabilization at 37°C

The superimposition of force-distance curves recorded for β_2AR and other GPCRs is highly reproducible and sensitive to experimental conditions (*29, 38, 42, 46*). To characterize how temperature influences the stability of the human β_2AR, we used SMFS to record many force-distance curves at 25°C, 37°C, and 42°C (Fig. 2). For β_2AR embedded in DOPC membranes, the force-distance curves revealed considerable temperature dependency (Fig. 2, A to C). The force peaks at contour lengths ≤ 135 amino acid residues (≤ 40 nm) were largely reduced in magnitude and distributed randomly upon increasing the temperature from 25°C to 37°C (Fig. 2, A and B). The substantial change of the first force peaks of the force-distance curves suggests the destabilization of the TMHs and polypeptide loops of the N-terminal half of the β_2AR (Fig. 1D). Upon further increasing the temperature to 42°C, all force peaks had reduced magnitude and were distributed randomly, thus indicating that the entire secondary structure of β_2AR was destabilized (Fig. 2, G to I). These results show that human β_2AR embedded in DOPC membranes destabilizes considerably at 37°C and higher temperatures.

Next, we characterized the temperature-dependent stability of human β_2AR embedded in DOPC membranes supplemented with the cholesterol analog CHS (Fig. 2, D to I). Force-distance curves recorded at 25°C for β_2AR in DOPC:CHS resembled those recorded in DOPC, thus indicating that CHS had little effect on the number and position of the unfolding force peaks. (Fig. 2G). The observation that the unfolding force peaks remained unchanged in position suggests that the β_2AR stabilizes the same structural segments and thus exposes the same native fold in DOPC and DOPC:CHS membranes (*29*). However, the magnitude of the unfolding force peaks was slightly greater in the presence of CHS, which suggests that the mechanical stability of the β_2AR was

increased (Fig. 2, A and D, and fig. S3). At 37°C, the SMFS spectrum recorded in DOPC:CHS showed patterns very similar to those recorded at 25°C, thus revealing no considerable changes of β_2AR (Fig. 2, D and E). This finding indicates that the structural stability of β_2AR embedded in DOPC:CHS remains largely unaffected by increasing the temperature from 25°C to 37°C. Comparing the substantial change in force peaks assigned to the N-terminal region of β_2AR in DOPC with the force peaks detected for β_2AR in DOPC:CHS at 25°C (Fig. 2G) and 37°C (Fig. 2H) suggests that CHS protects this structural region against thermal destabilization.

Further increasing the temperature to 42°C changed the force-distance curves recorded for β_2AR in DOPC:CHS in a similar way as was observed for β_2AR in DOPC at 42°C (Fig. 2, C and F). In particular, the eight force peaks had reduced magnitudes and were distributed randomly, as was also indicated in the probability histogram of the force peaks (Fig. 2I). We can thus conclude that the presence of CHS in the phospholipid membrane moderately increases the mechanical stability of β_2AR at 25°C and protects the β_2AR from partially destabilizing at 37°C. However, CHS could not protect the β_2AR from destabilizing at 42°C. This thermal destabilization particularly affected the N-terminal structural region of β_2AR, which contains TMH1, TMH2, TMH3, and TMH4. Because these TMHs represent the consensus cholesterol-binding motif that predicts cholesterol binding for 44% of human class A GPCRs (*27*), these results suggest that the cholesterol analog CHS interacts with and stabilizes this structural region.

CHS modulates the free-energy landscape of the β_2AR nonlinearly with temperature

The unfolding force of proteins depends on the speed (time / loading rate) at which they are mechanically stressed (*47, 48*). Thus, their mechanical, energetic, and kinetic properties are better

described by the concept of a free-energy landscape (*47-52*). In the absence of any detailed information, the free-energy landscape stabilizing each structural segment of β_2AR against mechanical unfolding is best described by a simple, two-state model having a single unfolding barrier (Fig. 3A) (*49, 52*). To determine the parameters of the free-energy landscape of every structural segment of β_2AR in DOPC and DOPC:CHS membranes, we measured their unfolding forces as a function of loading rate at 25°C, 37°C, and 42°C by DFS (figs. S3 to S5). The loading-rate–dependent unfolding force of every structural segment of β_2AR was fitted with the Bell-Evans model (*49, 52, 53*) to reveal their free-energy landscape parameters (Fig. 3), including: (i) the distance between the folded and the transition state x_u, which describes the conformational flexibility (or variability) needed to adopt conformational substates; (ii) the transition rate k_0 or lifetime $1/k_0$; (iii) the stabilizing free-energy barrier ΔG; and (iv) the free-energy landscape roughness ε describing the energetic stability of conformational substates.

Cholesterol increases the conformational flexibility of the β_2AR at physiological temperature

At 25°C, the distance of the transition state x_u of each structural segment of β_2AR showed small differences in the absence and presence of CHS (Fig. 3B). In the presence of CHS, the two structural segments S1 and S2 increased x_u moderately from 0.12 to 0.25 nm and 0.15 to 0.25 nm, respectively. At 37°C, however, six of eight structural segments had decreased x_u values in DOPC, whereas S1, S2, S4, S5, and S6 increased their x_u values substantially in the presence of CHS. Although the remaining segments S3, S7, and S8 also showed a tendency to increase their x_u values in CHS, the increase was not statistically significant. Markedly, the x_u values from the structural segments S1, S2, S5, and S6 ranged from 0.15 to 0.21 nm in DOPC and from 0.49 to 1.01 nm in DOPC:CHS. The biggest difference was observed for segments S1 and S5, which, in the presence

of CHS, increased x_u ~six-fold to 1.01 and 0.9 nm, respectively. This observation shows that in the presence of CHS at 37°C, five of eight structural segments of β_2AR increased their transition state x_u and thus their conformational flexibility (Fig. 3B and fig. S4). Upon further increasing the temperature to 42°C, the structural segments had substantially decreased x_u values ($\leq$ 0.2 nm), which was independent of the presence of CHS. At 42°C, no significant differences in x_u values were observed among the structural segments in DOPC and DOPC:CHS.

Cholesterol modulates the functional states of various GPCRs (*21, 54, 55*), whereas the depletion of cholesterol from the membrane of neonatal cardiac myocytes alters the signaling behavior of endogenous β_2AR (*56*). NMR and double-electron resonance studies revealed substantial conformational heterogeneity of the β_2AR in the apo state (*10*). Such heterogeneity gives rise to conformational substates between which β_2AR must transition to exhibit basal activity (*10*). Our results show that in the absence of CHS, the β_2AR is exposed to a narrowed conformational space, which implies that the receptor cannot adopt all of the conformational substates available to the β_2AR exposed to cholesterol. Such a reduction in the multi-state free-energy landscapes was previously predicted to illustrate how GPCRs lose function (*51*). The observed structural flexibility of segments S1, S2, S5, and S6 in the presence of CHS at 37°C may be interpreted in terms of their relevance for the β_2AR structure-function relationship. For example, the segments S5 and S6 stabilize TM5 and TM6, and β_2AR transiting from the inactive to the active state shows large structural outward movements of TMH6 and TMH5, whereas TMH5 extends its α-helix towards the cytoplasm (*57*). On the other hand, TMH1, whose properties are described by segments S1 and S2, is a part of binding pocket for allosteric ligands, which modulate the activity of

neurotransmitters and hormones (*58*). Our results thus suggest that cholesterol assists β_2AR in maintaining a wide conformational space at 37°C, as is required for receptor function (*51*).

Cholesterol increases the lifetime of the β_2AR

At 25°C in DOPC, the first three N-terminal structural segments S1, S2, and S3 showed transition rates k_0 ranging from 1.6 to 7.2 s^{-1}. They hence exposed considerably lower kinetic stabilities compared to segments S4 to S8, whose transition rates ranged from 10^{-4} to 10^{-1} s^{-1} (Fig. 3C). In DOPC:CHS, the kinetic stability of all structural segments exhibited k_0 values ranging from 10^{-4} to 10^{-1} s^{-1}, thus indicating that the presence of CHS increased the kinetic stability of structural segments S1, S2, and S3 of β_2AR. At 37°C, most structural segments of β_2AR embedded in DOPC exhibited substantial increases in their k_0 values, with structural segments S2, S3, S4, and S5 showing the highest values. This result indicates that the β_2AR in DOPC has reduced kinetic stability at 37°C compared to that at 25°C. In the presence of CHS, however, the transition rates of all structural segments remained considerably low, ranging from 10^{-11} to 10^{-1} s^{-1}, which indicates that CHS kinetically stabilized the β_2AR. The highest kinetic stabilization was observed for segments S1, S2, S5, and S6. At 42°C, all structural regions of the receptor exhibited substantial increases in their transition rates regardless of whether the receptor was embedded in DOPC or DOPC:CHS. Together, the results show that CHS kinetically stabilizes β_2AR at 25°C and protects the receptor from kinetic destabilization at 37°C. However, this stabilizing effect of CHS is lost at 42°C.

The observation that the transition rates of the structural segments of β_2AR increase with temperature is similar to what has been described for bacteriorhodopsin (*59*). Because β_2AR shows structural homologies to bacteriorhodopsin and class A GPCRs, the results suggest that increasing the

temperature within the physiological range can kinetically destabilize GPCRs. Although this effect may not hold for the structurally and functionally thermostable transmembrane protein bacteriorhodopsin (*60*), it is obviously prominent for the structure-function relationship of GPCRs, which are sensitive to much smaller temperature variations (*28, 30, 61*). For example, the melting temperature of the apelin receptor (APJ), a class A GPCR, lies at ~43°C in the absence of CHS (*30*). In addition, isothermal denaturation assays in the presence of the strong denaturant GnHCl revealed an 8-fold increased stability of β_2AR at 35°C in the presence of CHS (*27*). Our finding that CHS kinetically stabilizes the β_2AR structure is in general agreement with such findings. However, our results indicate that the action of CHS on β_2AR is likely tailored to the physiological temperature of 37°C. In particular, the properties of individual structural segments of β_2AR embedded in CHS-containing membranes change nonlinearly with temperature.

Cholesterol increases the energetic stability of the β_2AR

The free-energy barriers stabilizing individual structural segments of β_2AR at 25°C ranged from 16.4 to 26.0 k_BT in DOPC and from 19.0 to 26.6 k_BT in DOPC:CHS (Fig. 3D). At room temperature, the presence of CHS had no considerable effect in energetically stabilizing the structural regions of β_2AR. However, at 37°C, the free-energy barriers of most of the structural segments were reduced in DOPC, ranging from 16.9 to 19.9 k_BT, whereas they increased in DOPC:CHS to values ranging from 19.0 to 41.7 k_BT. In particular, the energetic stability of segments S1, S2, S5, and S6 increased considerably. At 42°C, the stabilizing effect of CHS was lost and the free-energy barriers were reduced to values ranging from 16.0 to 17.8 k_BT in both DOPC and DOPC:CHS, which supports our initial observation that β_2AR became mechanically destabilized at 42°C (Fig. 2). In summary, these results show that CHS had no substantial effect in energetically stabilizing

β_2AR at 25°C and 42°C. However, CHS stabilized the receptor at 37°C. One may thus speculate that the functional impairment of β_2AR in the absence of cholesterol (*54, 56, 62*) may be due to the energetic destabilization of its structure.

Free-energy landscape roughness of the β_2AR structure

Using the free-energy landscape parameters approximated at 25°C and 37°C, we calculated the free-energy landscape roughness of each structural segment, ε, stabilizing β_2AR (Materials and Methods, Eq. 3) in the absence and presence of CHS (Table 1). This roughness is frequently used to describe the local minima of the free-energy landscape, which trap smaller conformational substates of protein structures (Fig. 3a). Thereby rougher free-energy landscapes suggest these smaller conformational substates to expose higher energetic stabilities (*59*). The roughness of most structural segments in the absence and presence of CHS ranged from 3.4 to 5.6 k_BT. However, in the presence of CHS, the structural segments S2 and S4 showed a rougher (difference > 1 k_BT) free-energy landscape of 4.6 *vs* 3.4 k_BT and 5.6 *vs* 4.5 k_BT, respectively.

The roughness of the free-energy landscape stabilizing the structural segments of β_2AR (~ 3 to 6 k_BT) was similar to that reported for segments of bacteriorhodopsin (~ 4 to 6 k_BT) (*59*). In the presence of CHS, the β_2AR segments S2 and S4, which represent the cytoplasmic end of TMH1, cytoplasmic loop C1, TMH2, and extracellular loop E1, exhibited substantial increases in their free-energy landscape roughness. This increase in roughness suggests that CHS energetically stabilizes the conformational substates of segments S2 and S4. This structural region of β_2AR, which is part of the consensus cholesterol-binding motif of human class A GPCRs, increases the packing constrains of GPCRs upon binding cholesterol (*27*). Similarly, TMH2 together with TMH4

increase helical packing in the presence of cholesterol, which serves as a bridge between both TMHs (*27*). Moreover, because TMH4 is considered to have the weakest fold in β_2AR (*27*), it can be assumed that the cholesterol bridging TMH2 and TMH4 contributes to the overall stabilization of β_2AR (Fig. 3).

MD simulations show segment-dependent interactions of CHS with the β_2AR

In our SMFS experiments, the mechanical unfolding of a single β_2AR takes from ~13 ms to ~265 ms depending on the cantilever speed. Although currently available computing resources in national supercomputing centers are exceptional, they do not enable us to atomistically simulate complex systems such as those studied here over the course of several ms. This implies that simulating the unfolding processes observed experimentally by SMFS is not possible unless one simulates the process at an accelerated speed, which may cause artifactual results because highly accelerated speeds unfold proteins far from thermal equilibrium (*63*). Given this point, we decided not to use atomistic simulations to explore the unfolding process itself. Instead, we used multi-microsecond simulations to gain insight into the molecular-scale mechanisms by which CHS affects the thermal stability and conformations of β_2AR. Such simulations can capture the spontaneous interaction events (associations and dissociations) of CHS and β_2AR, which enabled us to interpret the CHS-induced effects observed in our SMFS experiments. We thus performed multi-microsecond atomistic MD simulations of β_2AR embedded in DOPC and DOPC:CHS membranes (fig. S6) and calculated the time-correlation functions for the interaction of CHS with the structural segments (figs. S7).

The MD simulation models accounted for seven of the structural segments (S1 to S7) of β_2AR, because the C-terminal end, which in our experiments is described as segment S8, has structurally not been solved (*27, 36*). The volumetric maps showed CHS to preferentially interact with β_2AR at specific sites located at well-defined structural segments (Fig. 4A). In particular, CHS strongly interacted with structural segment S6, which consists of the intracellular parts of TMH5 and TMH6, and of their connecting loop C3. Note that structural segment S6 matches the position of the cholesterol hot spot IC2 as predicted by our previous simulations (*36*). There is also a high density of CHS observed between two structural segments S1 and S4, which overlaps with the low-affinity interaction site EC3 that was predicted for cholesterol (*36*). In addition, CHS also interacts with structural segment S7 and, to some extent, with structural segment S5, which confirms our previous work that the EC1 interaction site of cholesterol lies at S7 and partly at S5 (*36*).

The interaction times of CHS with β_2AR depend on the structural segment (Table 2 and fig. S7). In particular, the interaction time of CHS was greatest for segments S1, S4, S5, S6, and S7, which correlates with specific CHS interaction sites revealed by volumetric maps of the CHS density (Fig. 4A). Moreover, the interaction energies revealed strong interactions of CHS with the structural segments S1, S4, S5, S6, and S7 of β_2AR (Fig. 4B). These pronounced interactions of CHS with certain structural segments of the receptor may explain why in our SMFS experiments we observed them to be mechanically, kinetically, and energetically stabilized. One exception was segment S2, for which the MD simulations could not explain the experimentally observed stabilization by CHS. We hence speculate that segment S2 may be stabilized by indirect effects of cholesterol on the lipid bilayer properties, such as the modulation of the mechanical properties of the

membrane. Together, the MD simulations suggest how membrane-embedded CHS may interact preferentially with certain functionally important regions of β_2AR.

To learn about the conformational space explored by β_2AR, we performed a principal component analysis (PCA) of the fluctuations of each structural segment for each given temperature (fig. S8 and Fig. 4C). The spread of the fluctuations was calculated by the two major principal components, PC1 and PC2, in the membrane plane. At 25°C, β_2AR exhibits similar structural flexibilities in the presence and absence of CHS. Similarly, at 42°C, CHS does not affect the structural flexibility of β_2AR significantly. However, at 37°C, the presence of CHS increases the structural flexibility of segment S6, and partially also segments S5 and S7, which supports our experimental findings.

General overview of temperature-dependent structural properties of β_2AR

To provide a general overview of the temperature-dependent β_2AR stabilization by CHS, the structural properties of β_2AR quantified *via* SMFS in the presence and in the absence of CHS (Fig. 3) were mapped onto the β_2AR structure (Fig. 5). The conformational variability, kinetic and energetic stability detected at 25°C, 37°C and 42°C bring our above described findings together, which will be to discussed in the following chapter.

DISCUSSION

Upon increasing temperature in the absence of CHS, the experimentally determined unfolding pattern of β_2AR reduced force and became noisy (Fig. 2). Both effects describe the destabilization of various structural regions of β_2AR. At 37°C, mostly the structural segments of the N-terminal region of β_2AR (TMH1 to TMH5) were destabilized and exhibited low kinetic stabilities (Fig. 5).

In the presence of CHS, this structural region of β_2AR, which contains the consensus cholesterol-binding motif of human class A GPCRs (*27*), was substantially stabilized. However, because cholesterol also modulates the mechanical properties of the membrane, one may speculate that these mechanical properties may modulate the β_2AR stability as well (*64*). In our SMFS experiments, we characterized the outcomes of both effects, the direct effects resulting from physicochemical interactions and the indirect effects resulting from the mechanical properties of the lipid membrane on the stability of the β_2AR.

In the absence of CHS, the conformational flexibility of the structural segments of β_2AR decreased with increasing temperature from 25°C to 37°C and 42°C (Fig. 5). The decreasing flexibility indicates that the number of conformational states of the receptor were reduced, which is consistent with the picture of kinetic and energetic destabilization of β_2AR (Fig. 5, C and D). However, in the presence of CHS, the conformational flexibility of β_2AR increased upon increasing temperature from 25°C to 37°C. Simultaneously, the kinetic and energetic stabilities of the receptor increased. At the further increased temperature of 42°C, all three parameters, the conformational flexibility, kinetic stability, and energetic stability of β_2AR exposed to CHS decreased substantially to values that were observed for the destabilized receptor in the absence of CHS. Thus, CHS modulates the structural properties of β_2AR specifically at 37°C. At all three temperatures investigated, MD simulations showed similar probability distributions for the interactions of CHS with β_2AR (Fig. 4A). However, CHS interacted with the structural segments S1, S5, S6, and S7 for greater times (Table 2, fig. S7). Overall, the atomistic MD simulations support the experimentally observed nonlinear stabilization of β_2AR by CHS.

Our experiments and simulations indicate that CHS stabilizes specific structural regions of human β_2AR. The largest CHS effects on energetic and kinetic stabilization and conformational space were observed for structural regions that are of importance for β_2AR signaling (TMH5, intracellular loop 3, and TMH6) and the binding of allosteric ligands (TMH1, TMH2, TMH6, and TMH7) (*58*). The stabilization of these structural regions was particularly effective at 37°C, which is physiologically the most relevant temperature for β_2AR. At 42°C, the protective function of CHS was lost and the β_2AR became destabilized. Whereas this type of destabilization may not necessarily lead to immediate thermal denaturation of β_2AR, it most probably affects the structure-function relationship of the receptor. This nonlinearity suggests that our understanding of how CHS modulates the structural properties of a GPCR at 25°C cannot be necessarily projected to describe how CHS modulates the receptor at 37°C or 42°C. More generally, it is essential to characterize the action of cholesterol on GPCRs at physiologically relevant temperatures. Given the structural and functional homology of GPCRs (*65*), we suggest that our findings about how temperature and cholesterol modulate the structural properties of β_2AR nonlinearly may be generalized to other class A GPCRs.

In the future, the combination of experimental SMFS studies and theoretical MD simulations presented here may be applied to systematically quantify how functionally or disease-related point-mutations modulate the CHS-promoted temperature-dependent (de-)stabilization of specific structural regions of the β_2AR. Hereto, point mutations of the key residues in the consensus cholesterol-binding motif and in functionally important structural regions may represent promising targets to start with.

MATERIALS AND METHODS

β_2AR subcloning, expression, purification, and reconstitution

Human β_2AR was expressed and purified as described previously (*66*). Briefly, β_2AR with a truncated C-terminal end (48 aa) and an N-terminal FLAG epitope followed by a tobacco etch virus (TEV) protease cleavage site was expressed in *Spodoptera frugiperda* (Sf9) insect cells for ~48 hours. To facilitate protein expression, we used a C-terminal truncated β_2AR construct, which does not affect β_2AR signaling (*57*). Successful expression of β_2AR was evaluated by immunofluorescence. Cells expressing β_2AR were harvested by centrifugation at 5000*g* for 15 min and stored at −80°C. To purify β_2AR from Sf9 cells, a three-step purification procedure was used. β_2AR was reconstituted in DOPC:CHS (10:1, vol:vol) or DOPC lipid vesicles as described previously (*66*). Briefly, a lipid:β_2AR mixture was mixed with reconstitution buffer and kept on ice for 2 hours. The lipid to protein ratio was 1000:1 (mol:mol). Detergent was removed with a 25 × 0.8 cm Sephadex G-50 (fine) column and reconstitution buffer [100 mM NaCl, 20 mM Hepes (pH 7.5)].

SMFS

β_2AR samples were aliquoted and flash-frozen in liquid nitrogen. For each SMFS experiment, a new sample was thawed freshly and used once. Proteoliposomes of β_2AR reconstituted in DOPC or DOPC:CHS (10:1, wt:wt) were adsorbed to the freshly cleaved surface of mica in SMFS buffer solution [300 mM NaCl, 25 mM $MgCl_2$, 25 mM Tris (pH 7.0)] for 1 hour. After the adsorption time passed, the samples were washed several times with SMFS buffer to remove weakly attached membrane patches. SMFS was performed at 25°C, 37°C, and 42°C using fully automated AFM (Force Robot 300, JPK Instruments) and a temperature-controlled sample holder (High

temperature heating stage, JPK Instruments). Every freshly thawed β_2AR sample was characterized by SMFS for a maximum of 5 hours after preparation and thereafter discarded. Data for different temperatures and lipid compositions were recorded in random order. 60 μm-long silicon nitride cantilevers (A-BioLever, BL-RC150VB, Olympus, Japan) were calibrated in SMFS buffer before and after each SMFS experiment with the equipartition theorem. SMFS was recorded at different speeds of cantilever retraction (300, 600, 900, 1200, 2500, and 5000 nm s^{-1}). Data at 2500 and 5000 nm s^{-1} were recorded with an external 16-bit data acquisition card (NI PCI-6221, National Instruments).

SMFS data analysis

In total ~6×10^6 force-distance curves from more than 300 independent SMFS experiments were recorded for this work over the time course of five years. A mechanically fully unfolded and stretched β_2AR extends to distances of 70 to 90 nm (*29, 38*). Thus, only force-distance curves showing a force peak pattern extending to distances >70 nm were selected for analysis. Consistent with previous results (*29, 38*), we observed the N-terminal end of the β_2AR to predominantly attach to the AFM stylus compared to the C-terminus (72%, $n = 210$). For statistical reasons, we hence focused on the analysis of force-distance curves, which recorded the mechanical unfolding of β_2AR from the N-terminal end. At least 100 force-distance curves recording the mechanical unfolding from the N-terminal end were analyzed for each unfolding speed to minimize the standard error of the mean (SEM). Every selected force-distance curve was then fitted by applying the worm-like-chain (WLC) model, with a persistence length of 0.4 nm and a contour length of 0.36 nm per amino acid residue (*67*). This WLC fit of each unfolding force peak provided the rupture force required to mechanically unfold a structural segment, as well as the contour length (in amino

acid residues) of the unfolded and stretched polypeptide. All contour lengths and rupture forces of all unfolding force peaks were grouped and analyzed for each experimental condition. Each unfolding force peak assigns the beginning and end of a structural segment stabilizing the unfolding β_2AR structure. The eight main force peaks detected were mapped to the secondary structure of β_2AR as described previously (*29, 38*). To locate the force peaks within or on the opposite side of the lipid membrane relatively to the pulling AFM cantilever, a membrane thickness of ~4 nm, which corresponds to the contour length of an ~11 amino acid residue–long polypeptide stretch, has been considered to approximate the total contour length of the unfolded and stretched polypeptide (*45, 68, 69*). In this so-called "membrane compensation, " the contour length of the unfolded and stretched polypeptide such as was estimated by fitting the force peak with the WLC model is extended by the contour length corresponding to the membrane thickness. Furthermore, at the relatively low unfolding forces applied in our study, the highly conserved disulfide bridge between residues Cys^{106} and Cys^{191} of β_2AR remains intact (*38*). Because the polypeptide stretch held together by the much stronger disulfide bridge did not unfold in our SMFS experiments, it was not accounted to localize the contour length of the unfolded and stretched polypeptide to a structural segment of β_2AR.

Quantifying free-energy landscape parameters

According to the Bell-Evans model (*53*), the most probable unfolding force F^* is a function of the loading-rate r:

$$F^* = \frac{k_B T}{x_u} ln\left(\frac{x_u r}{k_B T k_0}\right) \qquad \text{Eq. 1}$$

where k_B is the Boltzmann constant and T the absolute temperature. The most probable unfolding force and loading-rate for every force peak (structural segment) at every speed were calculated taking the maximum of the Gaussian fit of the rupture force and loading-rate distributions. Applying Eq. 1, we then calculated x_u and k_0 for each structural segment depending on the lipid composition and temperature. The height of the free-energy barrier $\Delta G^{\ddagger}$ was calculated by applying Eq. 2:

$$\Delta G^{\ddagger} = -k_B T ln(\tau_A k_0) \qquad \text{Eq. 2}$$

Using the DFS parameters, we applied Eq. 3 to quantify the average roughness ε of the free-energy landscape in the presence and absence of CHS:

$$\varepsilon^2 \approx \frac{x_u(T_2)k_B T_2 x_u(T_1)k_B T_1}{x_u(T_2)k_B T_2 - x_u(T_1)k_B T_1}\left[\Delta G_u * \left(\frac{1}{x_u(T_1)} - \frac{1}{x_u(T_2)}\right) + \frac{k_B T_1}{x_u(T_1)} ln\left(\frac{r_f(T_1)x_u(T_1)}{k_0(T_1)k_B T_1}\right) - \frac{k_B T_2}{x_u(T_2)} ln\left(\frac{r_f(T_2)x_u(T_2)}{k_0(T_2)k_B T_2}\right)\right] \qquad \text{Eq. 3}$$

Statistical data analysis

Overall more than 300 independent SMFS experiments were performed to acquire the necessary statistics for each of the six experimental conditions (e.g., temperature and lipid composition). To access the statistical significance of the differences observed in the presence and absence of CHS, the slopes and intercepts of linear DFS fits were compared (figs. S3 to S5). A method equivalent to ANCOVA (*70*) and implemented in GraphPad Prism was used. Comparison of the slopes was used to access statistical significance for differences in x_u, and comparison of the intercepts was used to access statistical significance for differences in k_0. Differences were considered significant

when P values approached $*P < 0.1$, $**P < 0.05$ and mean values did not overlap within their SDs for x_u and ΔG, and their SDs after logarithmical transformation for k_0, because the distribution of k_0 is right-skewed (Fig. 3, B to D).

All-atom MD simulations

We performed atomistic MD simulations of β_2AR embedded in a DOPC lipid bilayer in the presence and absence of 10 mol% of CHS, at 25°C, 37°C, and 42°C (Fig. 5 and table S1). Systems explored in this work contained one β_2AR placed in a membrane composed of 202 to 338 lipid molecules. All systems were explicitly solvated by water together with counter ions added to achieve electroneutrality with 150 mM NaCl. Each system was first energy-minimized to remove bad contacts. After energy minimization, we simulated the systems for 25 to 50 ns with position restraints on the receptor heavy atoms and then for another 25 to 50 ns with position restraints only on the receptor backbone atoms. Subsequently, all restraints were released, and every system was subjected to 2.5 μs of simulation, with three simulation repeats for DOPC systems, and with six simulation repeats for DOPC:CHS systems (table S1). All simulations were performed with the GROMACS 5.0.4 package (*71*) using the all-atom OPLS-AA force field (*72*). Parameters for CHS were as described previously (*73*). As used previously for DOPC (*36*), we used torsional and Lennard-Jones parameters for saturated (*74*) and unsaturated hydrocarbons (*73, 75*) and the torsional potential for the glycerol backbone and the phospholipid head group (*74*). Water molecules were modelled with the TIP3P water model, which is compatible with OPLS parameterization (*76*). All simulations were performed in the isothermal-isobaric (NpT) ensemble. The v-rescale (stochastic velocity rescaling) thermostat (*77*), with a time constant of 0.1 ps, was used to maintain the simulation temperature. The temperatures of the β_2AR, lipids, and solvent (water and ions) were

controlled independently. The pressure of the systems was maintained at 1 bar with the Parrinello-Rahman barostat (*78*) with a time constant of 1 ps. A semi-isotropic scheme was used for pressure control. Simulations were performed with a time step of 2.0 fs. To preserve the lengths of covalent hydrogen bonds, the LINCS algorithm (*79*) was applied. Periodic boundary conditions were applied in all three directions. Van der Waals interactions were treated using the Lennard-Jones potential with a cut-off distance of 1.0 nm. Long-range electrostatic interactions were evaluated with the particle mesh Ewald algorithm (*80*) using a real space cut-off of 1.0 nm, a β-spline interpolation (order of 6), and a direct sum tolerance of 10^{-6}. The simulation model used was validated in an exhaustive series of >100-μs atomistic simulations (*36*).

SUPPLEMENTARY MATERIALS

Supplementary Methods
Figs. S1 to S8.
Table S1.

REFERENCES AND NOTES

1. S. Takeda, S. Kadowaki, T. Haga, H. Takaesu, S. Mitaku, Identification of G protein-coupled receptor genes from the human genome sequence. *FEBS Lett* **520**, 97-101 (2002).
2. R. Fredriksson, M. C. Lagerstrom, L. G. Lundin, H. B. Schioth, The G-protein-coupled receptors in the human genome form five main families. Phylogenetic analysis, paralogon groups, and fingerprints. *Mol Pharmacol* **63**, 1256-1272 (2003).
3. D. M. Rosenbaum, S. G. Rasmussen, B. K. Kobilka, The structure and function of G-protein-coupled receptors. *Nature* **459**, 356-363 (2009).
4. V. Katritch, V. Cherezov, R. C. Stevens, Structure-function of the G protein-coupled receptor superfamily. *Annu Rev Pharmacol Toxicol* **53**, 531-556 (2013).
5. V. Cherezov, D. M. Rosenbaum, M. A. Hanson, S. G. Rasmussen, F. S. Thian, T. S. Kobilka, H. J. Choi, P. Kuhn, W. I. Weis, B. K. Kobilka, R. C. Stevens, High-resolution crystal structure of an engineered human beta2-adrenergic G protein-coupled receptor. *Science* **318**, 1258-1265 (2007).
6. S. G. Rasmussen, B. T. DeVree, Y. Zou, A. C. Kruse, K. Y. Chung, T. S. Kobilka, F. S. Thian, P. S. Chae, E. Pardon, D. Calinski, J. M. Mathiesen, S. T. Shah, J. A. Lyons, M. Caffrey, S. H. Gellman, J. Steyaert, G. Skiniotis, W. I. Weis, R. K. Sunahara, B. K. Kobilka, Crystal structure of the beta2 adrenergic receptor-Gs protein complex. *Nature* **477**, 549-555 (2011).

7. T. R. Bai, Beta 2 adrenergic receptors in asthma: a current perspective. *Lung* **170**, 125-141 (1992).
8. R. J. Lefkowitz, The superfamily of heptahelical receptors. *Nat Cell Biol* **2**, E133-136 (2000).
9. A. Madamanchi, Beta-adrenergic receptor signaling in cardiac function and heart failure. *Mcgill J Med* **10**, 99-104 (2007).
10. A. Manglik, T. H. Kim, M. Masureel, C. Altenbach, Z. Y. Yang, D. Hilger, M. T. Lerch, T. S. Kobilka, F. S. Thian, W. L. Hubbell, R. S. Prosser, B. K. Kobilka, Structural Insights into the Dynamic Process of beta(2)-Adrenergic Receptor Signaling. *Cell* **162**, 1431-1431 (2015).
11. R. Dawaliby, C. Trubbia, C. Delporte, M. Masureel, P. Van Antwerpen, B. K. Kobilka, C. Govaerts, Allosteric regulation of G protein-coupled receptor activity by phospholipids. *Nat Chem Biol* **12**, 35-39 (2016).
12. L. Susac, M. T. Eddy, T. Didenko, R. C. Stevens, K. Wuthrich, A2A adenosine receptor functional states characterized by (19)F-NMR. *Proc Natl Acad Sci U S A* **115**, 12733-12738 (2018).
13. N. R. Latorraca, A. J. Venkatakrishnan, R. O. Dror, GPCR Dynamics: Structures in Motion. *Chem Rev* **117**, 139-155 (2017).
14. Y. L. Liang, M. Khoshouei, M. Radjainia, Y. Zhang, A. Glukhova, J. Tarrasch, D. M. Thal, S. G. B. Furness, G. Christopoulos, T. Coudrat, R. Danev, W. Baumeister, L. J. Miller, A. Christopoulos, B. K. Kobilka, D. Wootten, G. Skiniotis, P. M. Sexton, Phase-plate cryo-EM structure of a class B GPCR-G-protein complex. *Nature* **546**, 118-123 (2017).
15. I. Shimada, T. Ueda, Y. Kofuku, M. T. Eddy, K. Wuthrich, GPCR drug discovery: integrating solution NMR data with crystal and cryo-EM structures. *Nat Rev Drug Discov* **18**, 59-82 (2019).
16. J. Garcia-Nafria, Y. Lee, X. Bai, B. Carpenter, C. G. Tate, Cryo-EM structure of the adenosine A2A receptor coupled to an engineered heterotrimeric G protein. *Elife* **7**, (2018).
17. H. Y. Yen, K. K. Hoi, I. Liko, G. Hedger, M. R. Horrell, W. Song, D. Wu, P. Heine, T. Warne, Y. Lee, B. Carpenter, A. Pluckthun, C. G. Tate, M. S. P. Sansom, C. V. Robinson, PtdIns(4,5)P2 stabilizes active states of GPCRs and enhances selectivity of G-protein coupling. *Nature* **559**, 423-427 (2018).
18. S. H. Park, B. B. Das, F. Casagrande, Y. Tian, H. J. Nothnagel, M. Chu, H. Kiefer, K. Maier, A. A. De Angelis, F. M. Marassi, S. J. Opella, Structure of the chemokine receptor CXCR1 in phospholipid bilayers. *Nature* **491**, 779-783 (2012).
19. R. O. Dror, D. H. Arlow, P. Maragakis, T. J. Mildorf, A. C. Pan, H. Xu, D. W. Borhani, D. E. Shaw, Activation mechanism of the beta2-adrenergic receptor. *Proc Natl Acad Sci U S A* **108**, 18684-18689 (2011).
20. G. Gimpl, V. Wiegand, K. Burger, F. Fahrenholz, Cholesterol and steroid hormones: modulators of oxytocin receptor function. *Prog Brain Res* **139**, 43-55 (2002).
21. G. Gimpl, Interaction of G protein coupled receptors and cholesterol. *Chem Phys Lipids* **199**, 61-73 (2016).
22. K. Simons, D. Toomre, Lipid rafts and signal transduction. *Nat Rev Mol Cell Biol* **1**, 31-39 (2000).
23. T. K. Ray, V. P. Skipski, M. Barclay, E. Essner, F. M. Archibald, Lipid composition of rat liver plasma membranes. *J Biol Chem* **244**, 5528-5536 (1969).

24. Y. Lange, M. H. Swaisgood, B. V. Ramos, T. L. Steck, Plasma membranes contain half the phospholipid and 90% of the cholesterol and sphingomyelin in cultured human fibroblasts. *J Biol Chem* **264**, 3786-3793 (1989).
25. S. L. Liu, R. Sheng, J. H. Jung, L. Wang, E. Stec, M. J. O'Connor, S. Song, R. K. Bikkavilli, R. A. Winn, D. Lee, K. Baek, K. Ueda, I. Levitan, K. P. Kim, W. Cho, Orthogonal lipid sensors identify transbilayer asymmetry of plasma membrane cholesterol. *Nat Chem Biol* **13**, 268-274 (2017).
26. D. Lingwood, K. Simons, Lipid Rafts As a Membrane-Organizing Principle. *Science* **327**, 46-50 (2010).
27. M. A. Hanson, V. Cherezov, M. T. Griffith, C. B. Roth, V. P. Jaakola, E. Y. T. Chien, J. Velasquez, P. Kuhn, R. C. Stevens, A specific cholesterol binding site is established by the 2.8 angstrom structure of the human beta(2)-adrenergic receptor. *Structure* **16**, 897-905 (2008).
28. G. Gimpl, F. Fahrenholz, Cholesterol as stabilizer of the oxytocin receptor. *Biochim Biophys Acta* **1564**, 384-392 (2002).
29. M. Zocher, C. Zhang, S. G. Rasmussen, B. K. Kobilka, D. J. Muller, Cholesterol increases kinetic, energetic, and mechanical stability of the human beta2-adrenergic receptor. *Proc Natl Acad Sci U S A* **109**, E3463-3472 (2012).
30. A. I. Alexandrov, M. Mileni, E. Y. Chien, M. A. Hanson, R. C. Stevens, Microscale fluorescent thermal stability assay for membrane proteins. *Structure* **16**, 351-359 (2008).
31. J. J. Ruprecht, T. Mielke, R. Vogel, C. Villa, G. F. Schertler, Electron crystallography reveals the structure of metarhodopsin I. *EMBO J* **23**, 3609-3620 (2004).
32. Y. D. Paila, S. Tiwari, A. Chattopadhyay, Are specific nonannular cholesterol binding sites present in G-protein coupled receptors? *Biochim Biophys Acta* **1788**, 295-302 (2009).
33. T. Warne, R. Moukhametzianov, J. G. Baker, R. Nehme, P. C. Edwards, A. G. Leslie, G. F. Schertler, C. G. Tate, The structural basis for agonist and partial agonist action on a beta(1)-adrenergic receptor. *Nature* **469**, 241-244 (2011).
34. W. Liu, E. Chun, A. A. Thompson, P. Chubukov, F. Xu, V. Katritch, G. W. Han, C. B. Roth, L. H. Heitman, I. J. AP, V. Cherezov, R. C. Stevens, Structural basis for allosteric regulation of GPCRs by sodium ions. *Science* **337**, 232-236 (2012).
35. D. Sengupta, A. Chattopadhyay, Molecular dynamics simulations of GPCR-cholesterol interaction: An emerging paradigm. *Biochim Biophys Acta* **1848**, 1775-1782 (2015).
36. M. Manna, M. Niemela, J. Tynkkynen, M. Javanainen, W. Kulig, D. J. Muller, T. Rog, I. Vattulainen, Mechanism of allosteric regulation of beta2-adrenergic receptor by cholesterol. *Elife* **5**, e18432 (2016).
37. D. Sengupta, X. Prasanna, M. Mohole, A. Chattopadhyay, Exploring GPCR-Lipid Interactions by Molecular Dynamics Simulations: Excitements, Challenges, and the Way Forward. *J Phys Chem B* **122**, 5727-5737 (2018).
38. M. Zocher, J. J. Fung, B. K. Kobilka, D. J. Muller, Ligand-specific interactions modulate kinetic, energetic, and mechanical properties of the human beta2 adrenergic receptor. *Structure* **20**, 1391-1402 (2012).
39. C. A. Bippes, L. Ge, M. Meury, D. Harder, Z. Ucurum, H. Daniel, D. Fotiadis, D. J. Muller, Peptide transporter DtpA has two alternate conformations, one of which is promoted by inhibitor binding. *Proc Natl Acad Sci U S A* **110**, E3978-E3986 (2013).

40. T. Serdiuk, M. G. Madej, J. Sugihara, S. Kawamura, S. A. Mari, H. R. Kaback, D. J. Muller, Substrate-induced changes in the structural properties of LacY. *Proc Natl Acad Sci U S A* **111**, E1571-1580 (2014).
41. L. Ge, S. Villinger, S. A. Mari, K. Giller, C. Griesinger, S. Becker, D. J. Muller, M. Zweckstetter, Molecular Plasticity of the Human Voltage-Dependent Anion Channel Embedded Into a Membrane. *Structure* **24**, 585-594 (2016).
42. P. M. Spoerri, H. E. Kato, M. Pfreundschuh, S. A. Mari, T. Serdiuk, J. Thoma, K. T. Sapra, C. Zhang, B. K. Kobilka, D. J. Muller, Structural Properties of the Human Protease-Activated Receptor 1 Changing by a Strong Antagonist. *Structure* **26**, 829-838 e824 (2018).
43. B. Hildebrandt, P. Wust, O. Ahlers, A. Dieing, G. Sreenivasa, T. Kerner, R. Felix, H. Riess, The cellular and molecular basis of hyperthermia. *Crit Rev Oncol Hematol* **43**, 33-56 (2002).
44. E. J. Walter, S. Hanna-Jumma, M. Carraretto, L. Forni, The pathophysiological basis and consequences of fever. *Crit Care* **20**, 200 (2016).
45. D. J. Muller, A. Engel, Atomic force microscopy and spectroscopy of native membrane proteins. *Nat Protoc* **2**, 2191-2197 (2007).
46. S. Kawamura, M. Gerstung, A. T. Colozo, J. Helenius, A. Maeda, N. Beerenwinkel, P. S. Park, D. J. Muller, Kinetic, energetic, and mechanical differences between dark-state rhodopsin and opsin. *Structure* **21**, 426-437 (2013).
47. H. Janovjak, K. T. Sapra, A. Kedrov, D. J. Muller, From valleys to ridges: Exploring the dynamic energy landscape of single membrane proteins. *Chemphyschem* **9**, 954-966 (2008).
48. C. A. Bippes, D. J. Muller, High-resolution atomic force microscopy and spectroscopy of native membrane proteins. *Rep Prog Phys* **74**, 086601 (2011).
49. G. I. Bell, Models for the specific adhesion of cells to cells. *Science* **200**, 618-627 (1978).
50. H. Frauenfelder, S. G. Sligar, P. G. Wolynes, The energy landscapes and motions of proteins. *Science* **254**, 1598-1603 (1991).
51. X. Deupi, B. K. Kobilka, Energy landscapes as a tool to integrate GPCR structure, dynamics, and function. *Physiology (Bethesda)* **25**, 293-303 (2010).
52. E. Evans, Probing the relation between force - Lifetime - and chemistry in single molecular bonds. *Annu Rev Bioph Biom* **30**, 105-128 (2001).
53. E. Evans, Energy landscapes of biomolecular adhesion and receptor anchoring at interfaces explored with dynamic force spectroscopy. *Faraday Discuss* **111**, 1-16 (1998).
54. T. J. Pucadyil, A. Chattopadhyay, Role of cholesterol in the function and organization of G-protein coupled receptors. *Prog Lipid Res* **45**, 295-333 (2006).
55. J. Oates, A. Watts, Uncovering the intimate relationship between lipids, cholesterol and GPCR activation. *Curr Opin Struct Biol* **21**, 802-807 (2011).
56. Y. Xiang, V. O. Rybin, S. F. Steinberg, B. Kobilka, Caveolar localization dictates physiologic signaling of beta 2-adrenoceptors in neonatal cardiac myocytes. *J Biol Chem* **277**, 34280-34286 (2002).
57. S. G. Rasmussen, H. J. Choi, D. M. Rosenbaum, T. S. Kobilka, F. S. Thian, P. C. Edwards, M. Burghammer, V. R. Ratnala, R. Sanishvili, R. F. Fischetti, G. F. Schertler, W. I. Weis,

B. K. Kobilka, Crystal structure of the human beta2 adrenergic G-protein-coupled receptor. *Nature* **450**, 383-387 (2007).
58. X. Liu, S. Ahn, A. W. Kahsai, K. C. Meng, N. R. Latorraca, B. Pani, A. J. Venkatakrishnan, A. Masoudi, W. I. Weis, R. O. Dror, X. Chen, R. J. Lefkowitz, B. K. Kobilka, Mechanism of intracellular allosteric beta2AR antagonist revealed by X-ray crystal structure. *Nature* **548**, 480-484 (2017).
59. H. Janovjak, H. Knaus, D. J. Muller, Transmembrane helices have rough energy surfaces. *J Am Chem Soc* **129**, 246-247 (2007).
60. H. Janovjak, M. Kessler, D. Oesterhelt, H. Gaub, D. J. Muller, Unfolding pathways of native bacteriorhodopsin depend on temperature. *EMBO J* **22**, 5220-5229 (2003).
61. D. L. Gater, O. Saurel, I. Iordanov, W. Liu, V. Cherezov, A. Milon, Two classes of cholesterol binding sites for the beta2AR revealed by thermostability and NMR. *Biophys J* **107**, 2305-2312 (2014).
62. N. Ben-Arie, C. Gileadi, M. Schramm, Interaction of the beta-adrenergic receptor with Gs following delipidation. Specific lipid requirements for Gs activation and GTPase function. *Eur J Biochem* **176**, 649-654 (1988).
63. E. Evans, K. Ritchie, Dynamic strength of molecular adhesion bonds. *Biophys J* **72**, 1541-1555 (1997).
64. D. M. Engelman, Membranes are more mosaic than fluid. *Nature* **438**, 578-580 (2005).
65. A. J. Venkatakrishnan, X. Deupi, G. Lebon, C. G. Tate, G. F. Schertler, M. M. Babu, Molecular signatures of G-protein-coupled receptors. *Nature* **494**, 185-194 (2013).
66. J. J. Fung, X. Deupi, L. Pardo, X. J. Yao, G. A. Velez-Ruiz, B. T. Devree, R. K. Sunahara, B. K. Kobilka, Ligand-regulated oligomerization of beta(2)-adrenoceptors in a model lipid bilayer. *EMBO J* **28**, 3315-3328 (2009).
67. M. Rief, M. Gautel, F. Oesterhelt, J. M. Fernandez, H. E. Gaub, Reversible unfolding of individual titin immunoglobulin domains by AFM. *Science* **276**, 1109-1112 (1997).
68. M. Kessler, H. E. Gaub, Unfolding barriers in bacteriorhodopsin probed from the cytoplasmic and the extracellular side by AFM. *Structure* **14**, 521-527 (2006).
69. C. Moller, D. Fotiadis, K. Suda, A. Engel, M. Kessler, D. J. Muller, Determining molecular forces that stabilize human aquaporin-1. *J Struct Biol* **142**, 369-378 (2003).
70. J. H. Zar, *Biostatistical Analysis*. (Prentice Hall, ed. 2nd Edition, 1984).
71. D. Van Der Spoel, E. Lindahl, B. Hess, G. Groenhof, A. E. Mark, H. J. Berendsen, GROMACS: fast, flexible, and free. *J Comput Chem* **26**, 1701-1718 (2005).
72. W. L. Jorgensen, Maxwell, D.S.,Tirado-Rives, J Development and testing of the OPLS all-atom force field on conformational energetics and properties of organic liquids. *Journal of the American Chemical Society* **118**, 11225-11236 (1996).
73. W. Kulig, P. Jurkiewicz, A. Olzynska, J. Tynkkynen, M. Javanainen, M. Manna, T. Rog, M. Hof, I. Vattulainen, P. Jungwirth, Experimental determination and computational interpretation of biophysical properties of lipid bilayers enriched by cholesteryl hemisuccinate. *Bba-Biomembranes* **1848**, 422-432 (2015).
74. A. Maciejewski, M. Pasenkiewicz-Gierula, O. Cramariuc, I. Vattulainen, T. Rog, Refined OPLS All-Atom Force Field for Saturated Phosphatidylcholine Bilayers at Full Hydration. *J Phys Chem B* **118**, 4571-4581 (2014).
75. W. Kulig, M. Pasenkiewicz-Gierula, T. Rog, Cis and trans unsaturated phosphatidylcholine bilayers: A molecular dynamics simulation study. *Chem Phys Lipids* **195**, 12-20 (2016).

76. W. L. Jorgensen, J. Chandrasekhar, J. D. Madura, R. W. Impey, M. L. Klein, Comparison of Simple Potential Functions for Simulating Liquid Water. *J Chem Phys* **79**, 926-935 (1983).
77. G. Bussi, D. Donadio, M. Parrinello, Canonical sampling through velocity rescaling. *J Chem Phys* **126**, (2007).
78. M. Parrinello, A. Rahman, Polymorphic Transitions in Single-Crystals - a New Molecular-Dynamics Method. *J Appl Phys* **52**, 7182-7190 (1981).
79. B. Hess, H. Bekker, H. J. C. Berendsen, J. G. E. M. Fraaije, LINCS: A linear constraint solver for molecular simulations. *J Comput Chem* **18**, 1463-1472 (1997).
80. T. Darden, D. York, L. Pedersen, Particle Mesh Ewald - an N.Log(N) Method for Ewald Sums in Large Systems. *J Chem Phys* **98**, 10089-10092 (1993).
81. I. Bahar, R. L. Jernigan, Vibrational dynamics of transfer RNAs: comparison of the free and synthetase-bound forms. *J Mol Biol* **281**, 871-884 (1998).
82. L. Piao *et al.*, Molecular Dynamics Simulations of Wild Type and Mutants of SAPAP in Complexed with Shank3. *Int J Mol Sci* **20**, (2019).

Acknowledgments: We thank J. Thoma, P. Spoerri, and M. Zocher for encouraging and constructive comments. **Funding:** This work was supported by the Swiss National Science Foundation (SNF; grant 205320_160199 to D.J.M.), the NCCR Molecular Systems Engineering (D.J.M.), the Department of Biotechnology (Government of India) under the BioCARe Women Scientists scheme (no.BT/PR17981/BIC/101/576/2016 to M.M.), the Academy of Finland (Center of Excellence program to I.V. and W.K.), the Helsinki Institute of Life Science Fellow program (to I.V.), the Sigrid Juselius Foundation (to I.V.), the US National Institutes of Health (R01NS028471 to B.K.K.), and the European Research Council (Advanced Grant project CROWDED-PRO-LIPIDS to I.V.). We further acknowledge major computer resources granted by CSC – IT Centre for Science (Espoo, Finland). **Author contributions:** T.S., D.J.M., and B.K. designed the experiments. T.S. performed the SMFS experiments. M.M., W.K., and I.V. designed the MD simulations. M.M. performed the MD simulations. C.Z. cloned, expressed, purified, and reconstituted the β_2AR in DOPC and DOPC/CHS proteoliposomes. S.A.M. recorded the AFM and TEM images. All authors analyzed the experimental and simulation data and wrote the paper. **Competing interests:** B.K.K. is co-founder of and consultant of ConfometRx, Inc.. The other authors declare that they have no competing interests. **Data and materials availability:** All data needed to evaluate the conclusions of the paper are present in the paper or the Supplementary Material. The raw SMFS data is available in the Supplementary Material.

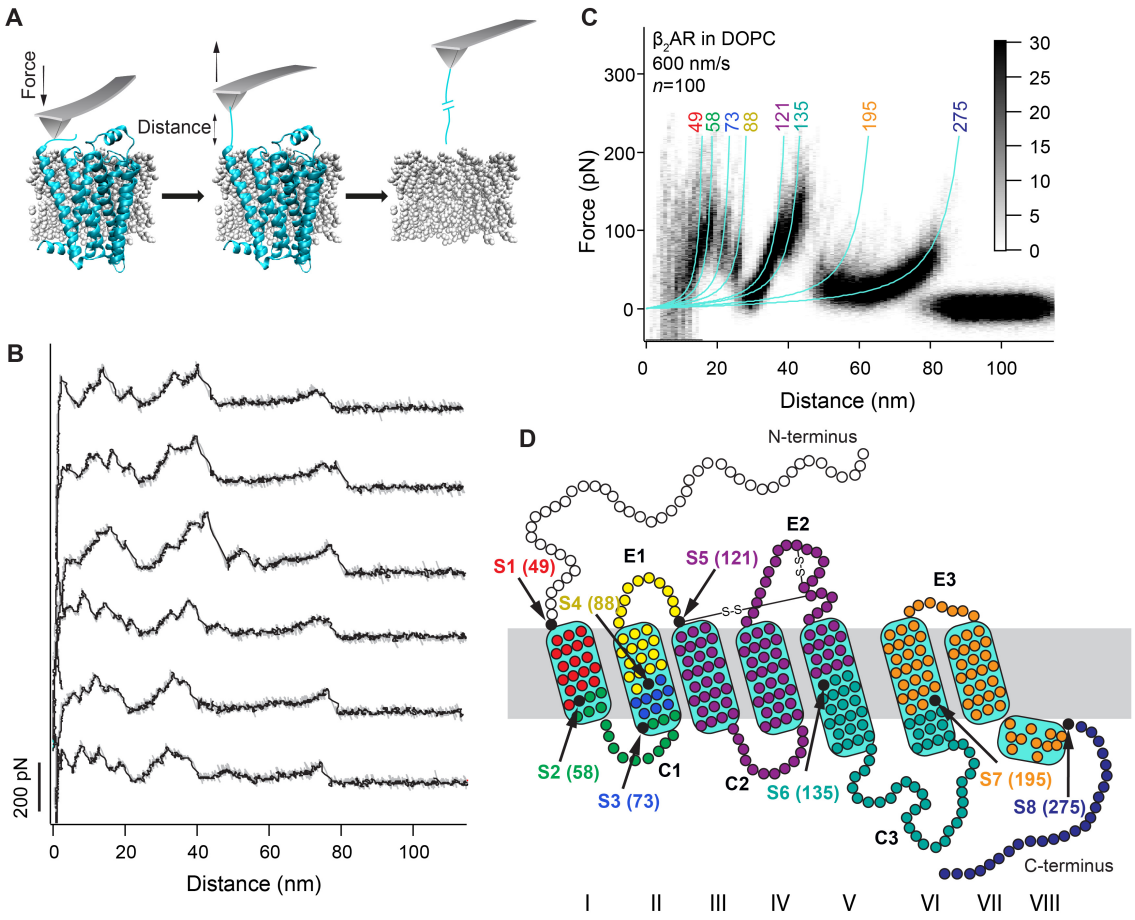

Fig. 1. SMFS analysis of the human β2AR reveals a common unfolding peak pattern. (**A**) Schematic representation of the SMFS experiment. The stylus of the AFM cantilever approaches to the surface of β2AR-containing proteoliposomes until reaching a contact force of 700 pN to nonspecifically attach to the N-terminus of individual receptors (*38*). After 0.5 s, the cantilever is retracted at constant speed and stretches the polypeptide linking the stylus and the β2AR. At sufficient mechanical force, β2AR unfolds stepwise until the polypeptide is completely extracted from the membrane. During this process, a force-distance curve is recorded. (**B**) Representative force-distance curves recorded upon mechanical unfolding of individual β2ARs from the N-terminal end at 25°C (*38*). (**C**) Superimposition of force-distance curves recorded upon unfolding of β2AR from a DOPC membrane. The density plot reveals a highly reproducible unfolding fingerprint pattern

of eight force peaks. Each force peak is fitted by the WLC model (gray lines; see Materials Methods) to approximate the contour length of the unfolded and stretched polypeptide. The mean contour lengths given at the top of each WLC curve in amino acids (aa) indicate where a structural segment starts unfolding and the unfolding of the previous structural segment ends. The gray scale bar of the density plot indicates the number of data points superimposed per bin. *n* gives the number of superimposed force-distance curves, which were recorded from more than 10 independent experiments. (**D**) The eight structural segments S1 to S8 mapped to the secondary structure of β_2AR. Helices are numbered with Roman numerals. Extrcellular (E1 to E3) and cytosolic (C1 to C3) loops are labelled. The linearized secondary structure was taken from the study of Zocher *et al*. (*38*) accordingly to tertiary structure model from Protein Data Bank (PDB) ID code 3D4S (*57*).

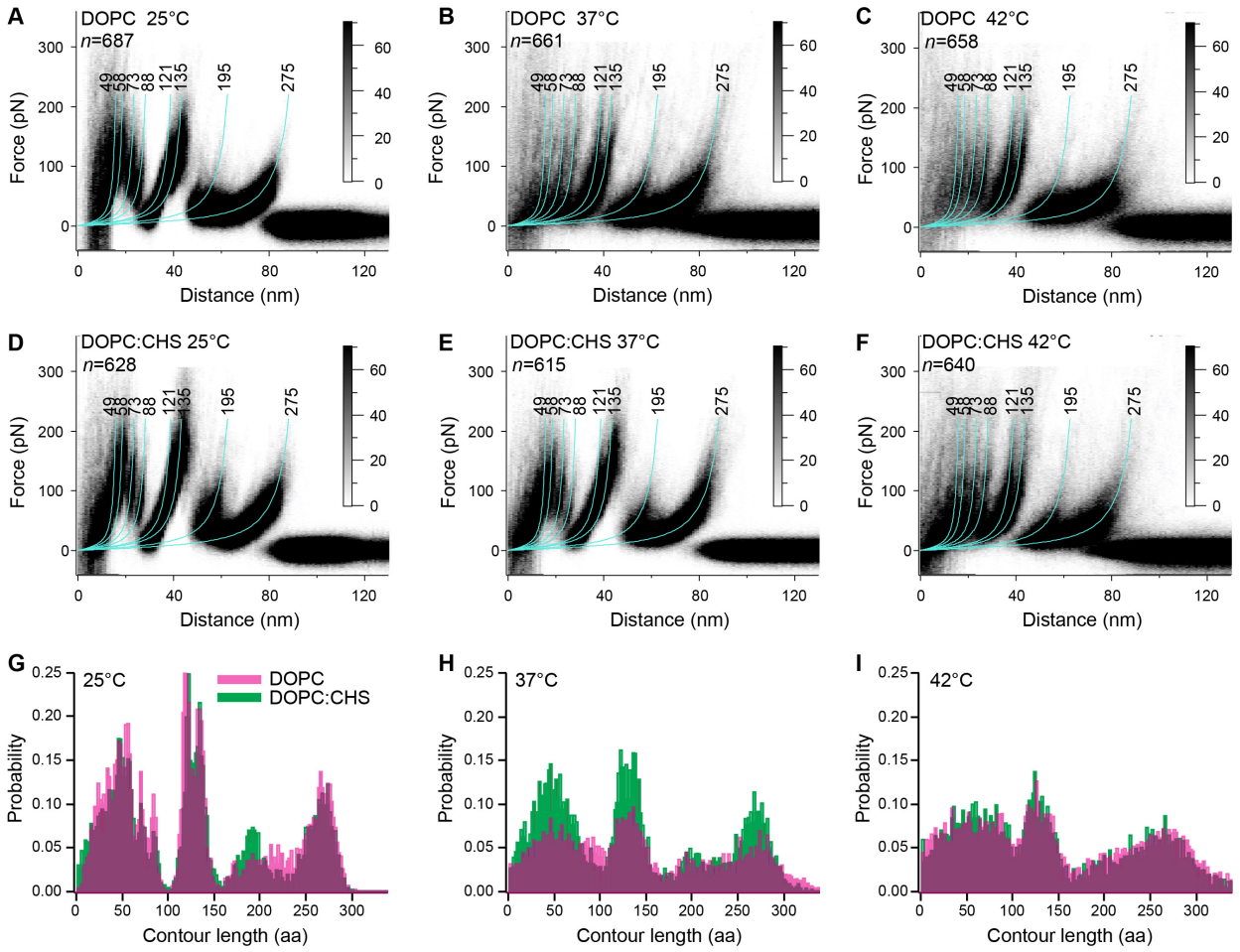

Fig. 2. The unfolding fingerprint pattern of human β2AR is sensitive to temperature. (**A** to **F**) Superimposed force-distance curves recorded upon the unfolding of β2AR from DOPC (A to C) and DOPC:CHS (D to F) lipid membranes at the indicated temperatures. Every density plot was compiled from force-distance curves recorded at six different unfolding speeds ranging from 300 nm/s to 5000 nm/s (see Materials and Methods). *n* gives the number of force-distance curves superimposed. (**G** to **I**) Contour length histograms mapping the occurrence of unfolding force peaks. The contour length of every unfolding force peak of every force-distance curve was determined as outlined in Fig. 1. The SMFS data were recorded upon the unfolding of β2AR embedded in DOPC (pink) and DOPC:CHS (green) membranes at 25°C (G), 37°C (H), and 42°C (I). For each experimental condition *n* gives the number of superimposed force-distance curves, which were recorded from more than 60 independent experiments.

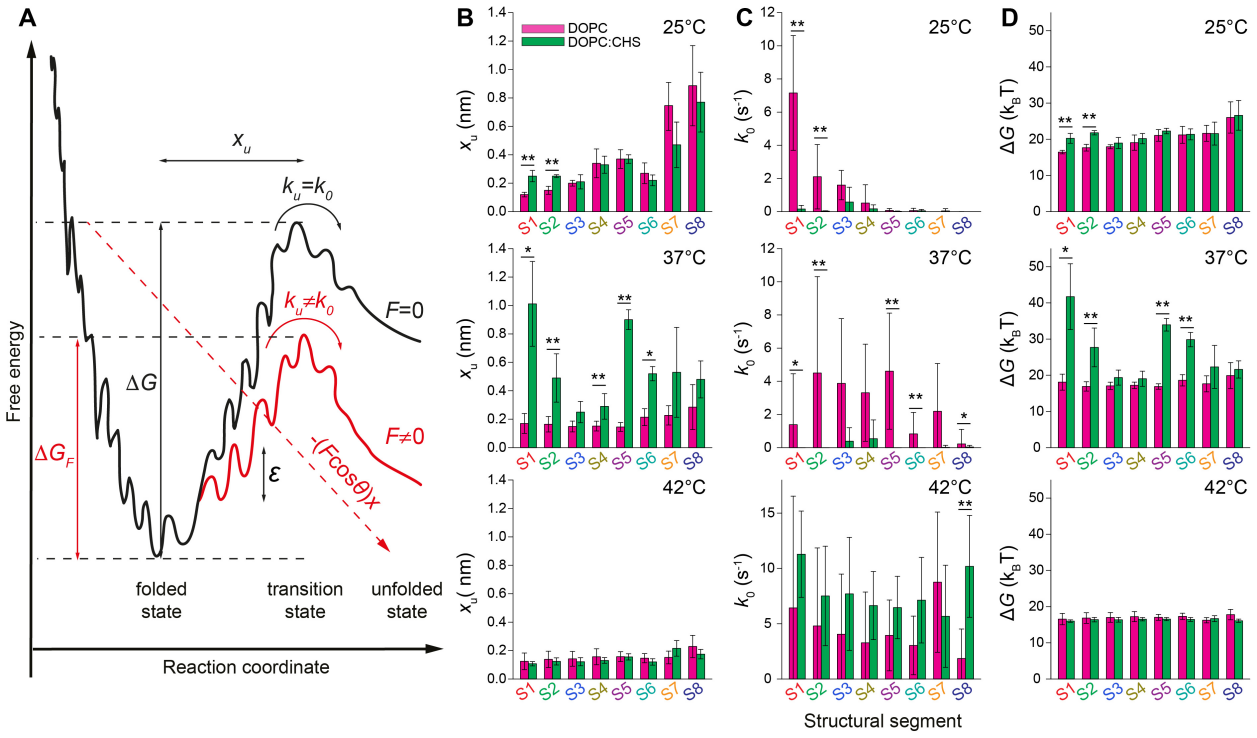

Fig. 3. Unfolding free-energy barrier stabilizing the structural segments of β2AR. (**A**) According to the Bell-Evans model (*52, 53*), a natively folded structure resides in a free-energy valley,

which is separated from the unfolded state by a free-energy barrier (black line). Unfolding the structure is initiated by overcoming the transition state of the free-energy barrier. x_u is the distance between the folded and transition states, k_0 is the transition rate to overcome the free-energy barrier ΔG in the absence of an external force (thermal equilibrium), and ε is the free-energy landscape roughness. Externally applying a mechanical force F reduces the thermal likelihood of the structure to reach the transition state. The free-energy projection along the reaction coordinate (pulling direction of the externally applied force) is tilted by the applied mechanical energy $-F(\cos\Theta)x$ (red dashed line), where Θ is the angle between reaction coordinate and the externally applied force. This tilt decreases the free-energy barrier height (red line), thereby increasing the probability of the folded structure to overcome the transition state towards unfolding. (**B**) Distance between the folded and transition state (x_u) of the structural segments S1 to S8 of the β_2AR embedded in DOPC and in DOPC-CHS. (**C**) Transition rates (k_0) of the structural segments S1 to S8 of the β_2AR embedded in DOPC and in DOPC-CHS. (**D**) The free-energy barrier height stabilizing each structural segment of the β_2AR embedded in DOPC and in DOPC-CHS. The values of parameters characterizing the free-energy landscape were obtained from fitting the Bell-Evans model to DFS plots recorded at 25°C, 37°C, and 42°C in the absence (pink) and in the presence (green) of CHS (see Materials and Methods, figs. S3 to S5). The raw data of the SMFS experiments, the number of force-distance curves analyzed and their analysis is given in Figs. 2 and 3. More than 300 independent experiments were performed over the time course of 5 years to acquire the necessary statistics (Materials and Methods). Statistical significance was determined by comparing the slopes and intercepts of linear regressions of the DFS plots in the presence and absence of CHS (figs. S3 to S5) by a method equivalent to ANCOVA (*70*). Differences were considered significant if P values approached $^*P < 0.1$ or $^{**}P < 0.05$ and if experimentally determined values did not overlap

within their SDs (A and C) or their SDs after logarithmical transformation of skewed k_0 distribution (B).

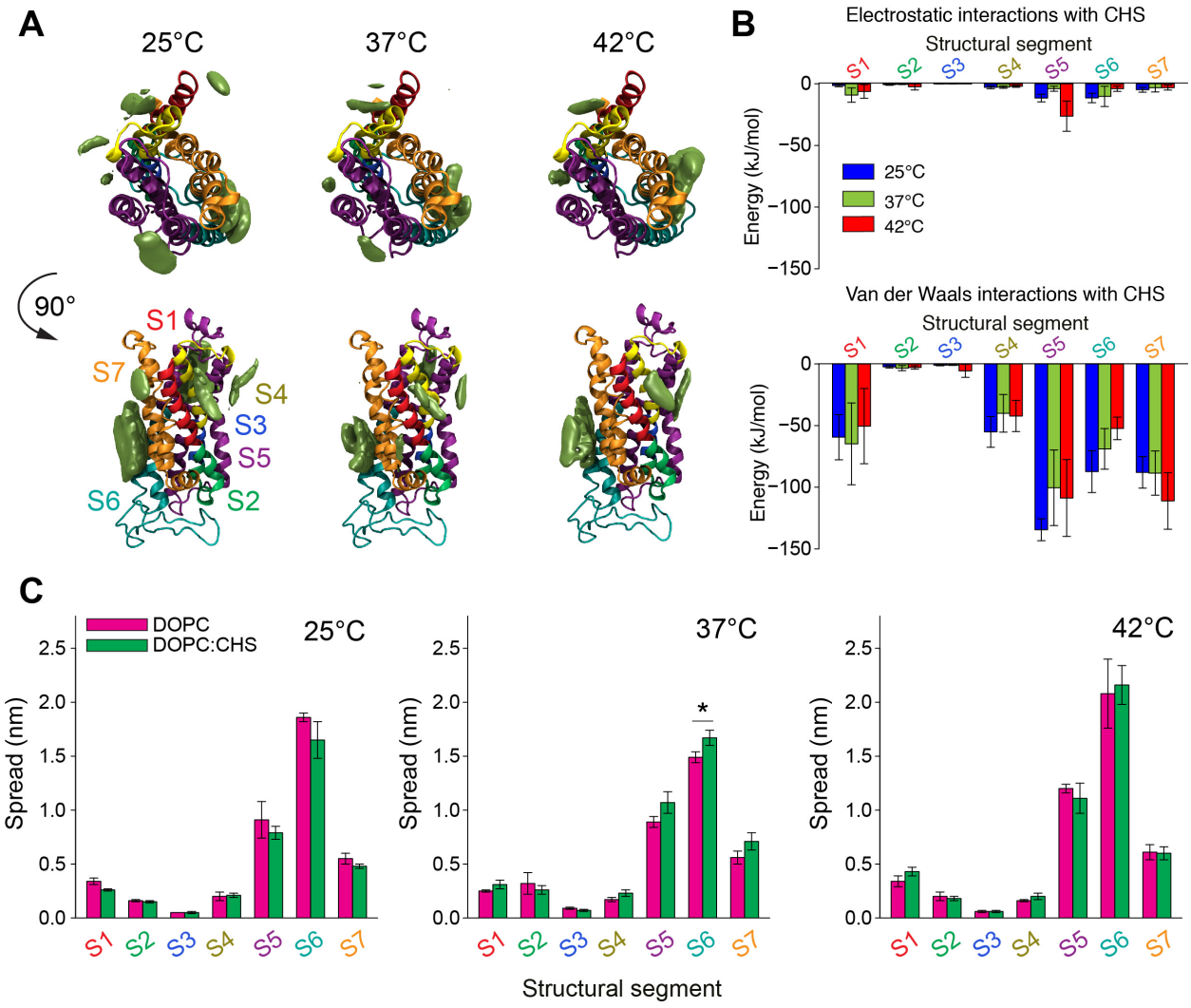

Fig. 4. Atomistic MD simulations of CHS interacting with structural segments of the human β₂AR. (**A**) Volumetric maps of the density of CHS (green surface) interacting with human β₂AR at 25°C, 37°C, and 42°C. At each temperature, the data were averaged from at least six independent trajectories (table S1). The structural segments of β₂AR are color-coded according to Fig. 1D. (**B**) Interaction energies resulting from the electrostatic (top) and van der Waals (bottom) interactions of CHS with the indicated structural segments of the human β₂AR at 25°C, 37°C, and 42°C. Bars and error bars of each structural segment show means ± SD (n ≥ 3, table S1). (**C**) Structural

fluctuations of the indicated structural segments of β_2AR projected along two major principle components parallel to the membrane plane. Bars describe the fluctuations of stable structural segments in the absence (pink) and in the presence (green) of CHS. The error (SD) of the spread estimation is <20%. For a description of the PCA used, see the Supplementary Materials. Differences were considered significant if *P* values approached *P<0.1 (calculated from a two-tailed t-test) and if the determined values did not overlap within their errors.

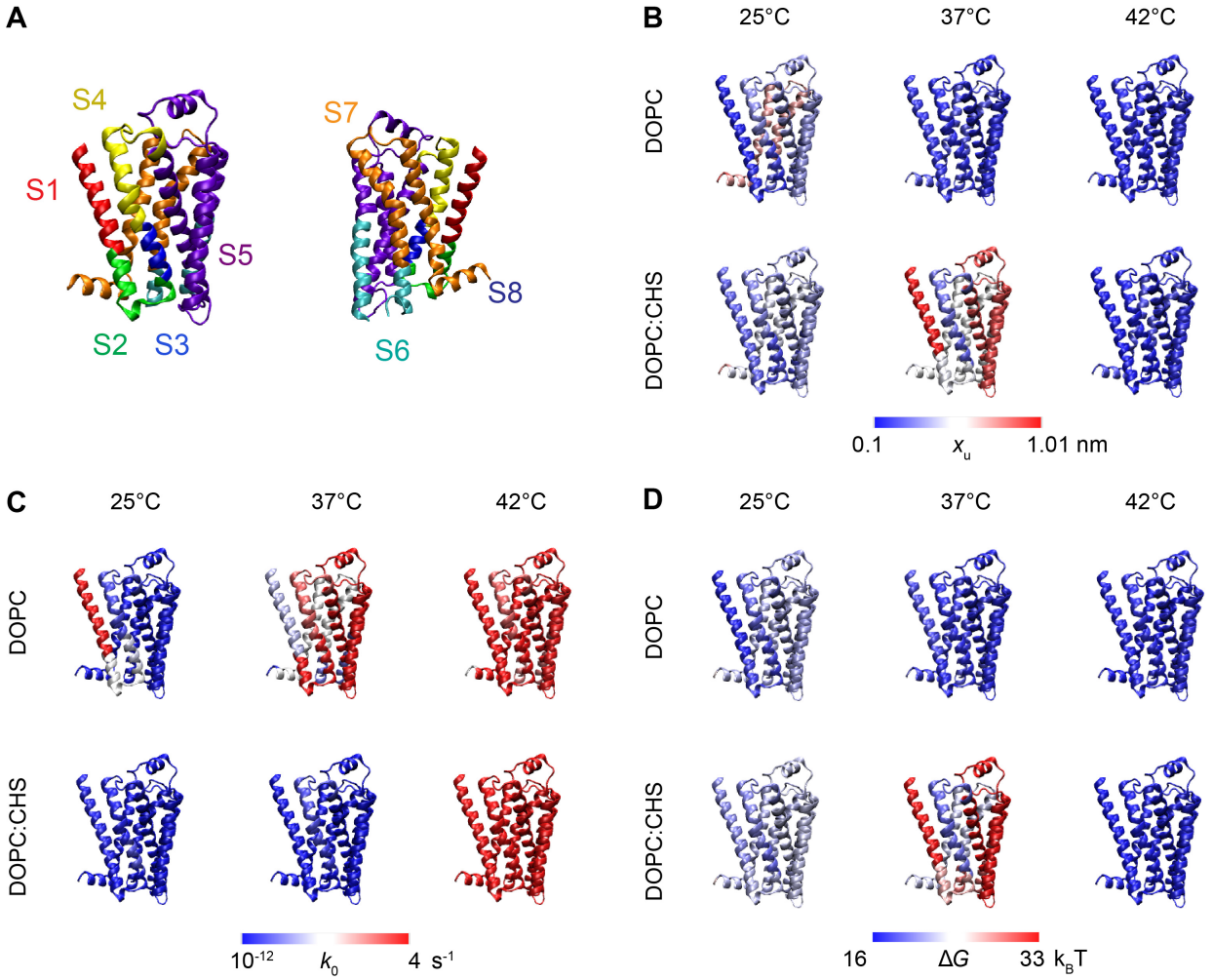

Fig. 5. Temperature-dependent kinetic and energetic properties of human β_2AR in the presence and absence of CHS. (**A**) Eight structural segments (taken from Fig. 1) mapped to the structure of human β_2AR [PDB ID: 3D4S; (*57*)]. (**B**) Distance between the folded and transition states,

x_u. (**C** and **D**) Transition rate k_0 (C) and height of the free-energy barrier ΔG (D) of the structural segments of β_2AR. The individual parameters are explained in Fig. 3 and their values were obtained from SMFS data recorded of β_2AR embedded in DOPC membranes in the absence and presence of CHS at 25°C, 37°C, and 42°C (Fig. 3).

Table 1. Energy landscape roughness ε of the structural segments of β_2AR in the absence and presence of CHS. ε values and SD values were calculated by applying Eq. 3 (Materials and Methods) to the DFS data recorded at 25°C and 37°C. Structural segments changing $\varepsilon > 1$ k_BT are marked by asterisks.

Structural segment	**DOPC (k_BT)**	**DOPC:CHS (k_BT)**
S1	3.9 ± 2.5	4.5 ± 1.0
S2*	3.4 ± 11.6	4.6 ± 1.6
S3	4.6 ± 1.9	4.0 ± 6.0
S4*	4.5 ± 1.4	5.6 ± 11.1
S5	4.8 ± 1.1	4.7 ± 0.6
S6	5.1 ± 5.9	4.5 ± 1.0
S7	4.8 ± 1.5	4.6 ± 19.6
S8	5.4 ± 2.9	5.5 ± 4.0
Mean ± SD of S1 to S8	4.6 ± 3.6	4.8 ± 5.6

Table 2. Interaction times of CHS with structural segments of the β_2AR as revealed from MD simulations. The average interaction times and SD values were calculated from the decay of time-correlation functions (fig. S7) by identifying the times when the time-correlation function was reduced to a value that was either 10 or 1% of the value at time zero. For the analysis shown here, we used data that were averaged over the six simulation repeats and the three simulation temperatures to maximize sampling and thus render the segment-based trend as clearly as possible.

Structural segment	**Interaction time (10%) (ns)**	**Interaction time (1%) (ns)**
S1	81.4 ± 21.5	284.5 ± 48.3
S2	17.7 ± 10.4	140.5 ± 65.0
S3	31.4 ± 31.0	231.8 ± 182.7
S4	111.8 ± 67.6	295.2 ± 88.8
S5	183.8 ± 52.8	410.9 ± 58.8
S6	129.3 ± 57.9	406.8 ± 203.1
S7	134.1 ± 66.1	492.8 ± 103.4
Mean ± SD of S1 to S7	98.5 ± 69.3	317.7 ± 157.1

Supplementary Methods

Simulation setup and analysis: β_2AR structure

The initial coordinates of the β_2AR (amino acid residues 32 to 342) were taken from our previous work (*36*), in which the structural modifications made for crystallization of the human β_2AR in its inactive state [PDB: 3D4S] (*27*) were reverted back to its pristine sequence. We therefore removed the mutations present in the crystal structure: the E122$^{3.41}$W mutation located in the transmembrane helix TMH3 and the N187$^{5.26}$E mutation located in the extracellular loop E2. Furthermore, because in the crystal structure the residues 231 to 262 of the intracellular loop C3 were substituted with a T4-lysozyme to facilitate experimental structure determination, we removed the T4-lysozyme attached between TMH5 and TMH6 and replaced it with the missing loop C3. The unresolved (and presumably disordered) N-terminal and C-terminal regions were not included in the simulation model. Details of the procedure used to prepare the receptor model for the simulations are discussed previously (*36*). Here, we used the final structure that resulted from this detailed preparation process.

Simulation setup and analysis: Embedding β_2AR in lipid membranes

In the present simulations, we used two different lipid compositions: a single-component DOPC membrane, and a DOPC membrane with 10 mol% CHS (table S1 and fig. S6). The apo-receptor was embedded into a pre-equilibrated (for 100 to 200 ns) lipid membrane in a manner whereby the initial lipid arrangement around the receptor was completely random. For each lipid composition, we prepared three different starting structures with a different organization of lipids around the β_2AR. Each of these six systems was simulated at 25°C, 37°C, and 42°C. In total, we performed 18 simulations, each covering a period of 2.5 μs, with a total simulation length of >45 μs.

Analyzing the interaction time of CHS with the structural segments (S1 to S7) on the receptor surface

We analysed the binding and unbinding events of each individual CHS molecule with the seven structural segments (S1 to S7) of the β_2AR. CHS was considered to be bound to a segment when the distance of any one of its atoms was ≤ 0.5 nm from any atom in the segment. After CHS bound to a structural segment, we determined the probability that CHS at a later time remained bound to the same segment by using the data of all individual binding and unbinding events to compute the (normalized) time-correlation function. The decay of the time-correlation function revealed the average interaction time of CHS binding (fig. S7). The trajectories of all simulation repeats were used for binding analysis.

Principal component analysis

Principal component analysis (PCA) is widely used to extract the essential dynamical motions of bio-molecules by filtering global and collective (often slow) motions from local and fast motions (*81*, *82*). To perform PCA, we first calculated the covariance matrix $\boldsymbol{C}$, where the matrix elements C_{ij} are defined as:

$$C_{ij} = < (x_i - < x_i >)(x_j - < x_j >) >$$

where x_i and x_j are the instant coordinates of the i^{th} and j^{th} atom, and $< x_i >$ and $< x_j >$ are the average coordinates of the respective atoms over the ensemble. By diagonalization and solving the eigenvalue and eigenvectors for the covariance matrix $\boldsymbol{C}$, we obtained the principal components (PCs). The eigenvectors of these PCs represent the directions of the motions, whereas the corresponding eigenvalues show the magnitudes of the motions along the given directions. Here, we used the g_covar and g_anaeig tools from the GROMACS package to perform the PCA analysis over the receptor backbone atoms. We projected our trajectory along the two main PCs (PC1 and PC2) in the membrane plane. An example of such analysis for structural segment S5 at 42°C is shown in fig. S8. Finally, the spread of these projections was calculated as the standard deviation (SD) from the barycenter of the distribution.

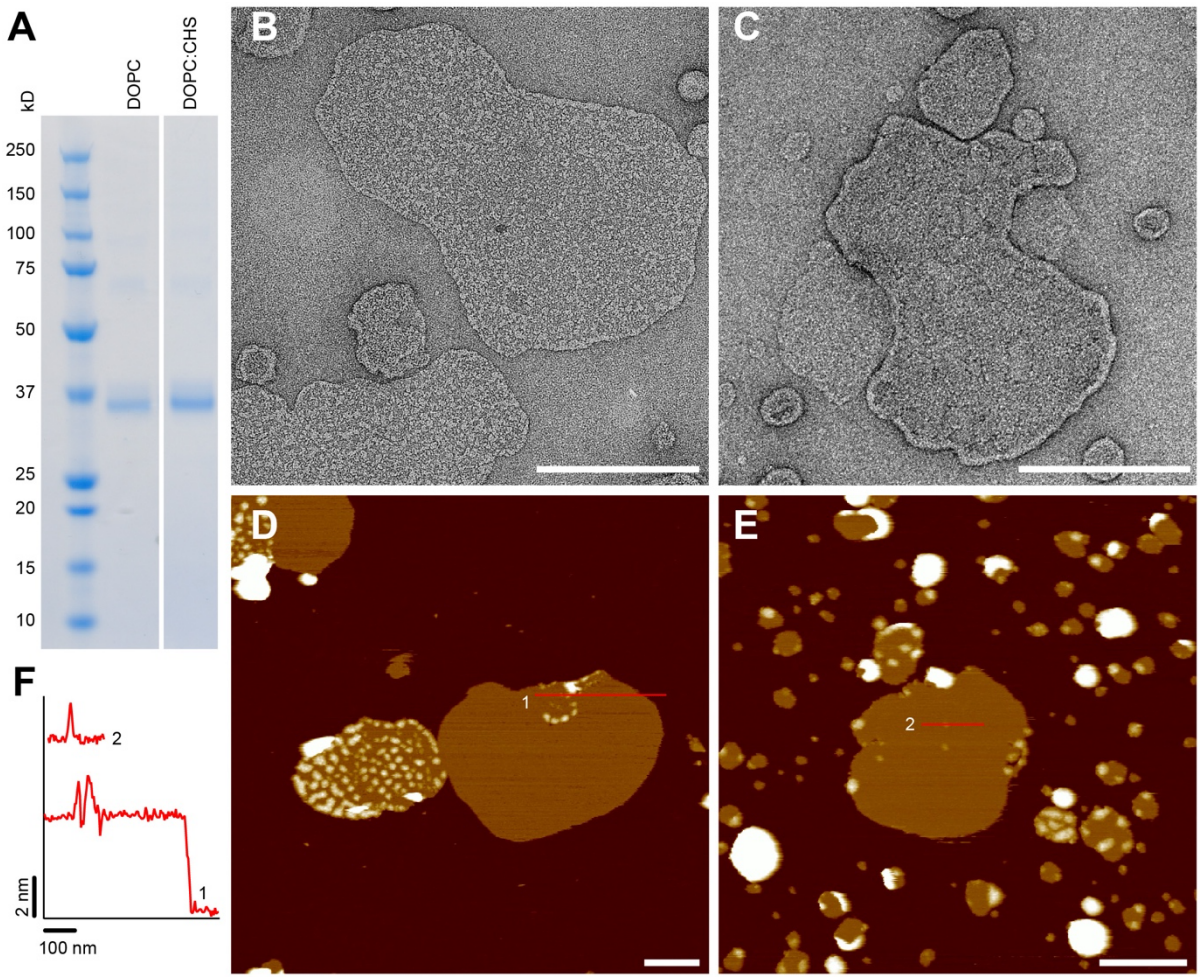

Fig. S1. Human β_2AR reconstituted in DOPC membranes in the presence and absence of CHS. (**A**) Coomassie blue–stained SDS gel (4 to 12%) of β_2AR reconstituted into DOPC liposomes (second lane) and DOPC:CHS liposomes (9:1, weight:weight, third lane). (**B** and **C**) TEM images of β_2AR reconstituted into DOPC (B) and DOPC:CHS (C) proteoliposomes. For TEM 5 µl proteoliposome solution was pipetted onto a glow-discharged copper grid coated with carbon. After an adsorption time of 1 min, the grid was washed with 4 droplets of milliQ water and subsequently stained with 2% (w/v) uranyl acetate for 10 s, blotting between each step. Grids were imaged using a transmission electron microscope (TEM) with a LaB6 filament operated at 120 kV (Tecnai G2 Spirit BioTWIN, FEI Company, Eindhoven, The Netherlands). Images were recorded by a side-mounted EMSIS MORADA camera. (**D** and **E**) AFM topographs of β_2AR in DOPC (D) and in DOPC:CHS (E) proteoliposomes adsorbed to mica. Upon attachment to mica, most of the proteoliposomes opened and adsorbed as single-layered membranes. (**F**) Height profile along the red lines on the AFM topographs (D and E). The membranes protruded ~5 to 6 nm above the mica surface and the smaller assemblies of membrane proteins protruded ~1 to 2 nm above the lipid membrane. Topographs were recorded by contact mode AFM in SMFS buffer solution and at room temperature as described previously (*45*). Scale bars, 200 nm. The full-range color range of the AFM topographs corresponds to vertical scales of 16 nm (D) and 16.5 nm (E). Each experiment shown has been repeated at least 3 times revealing similar results.

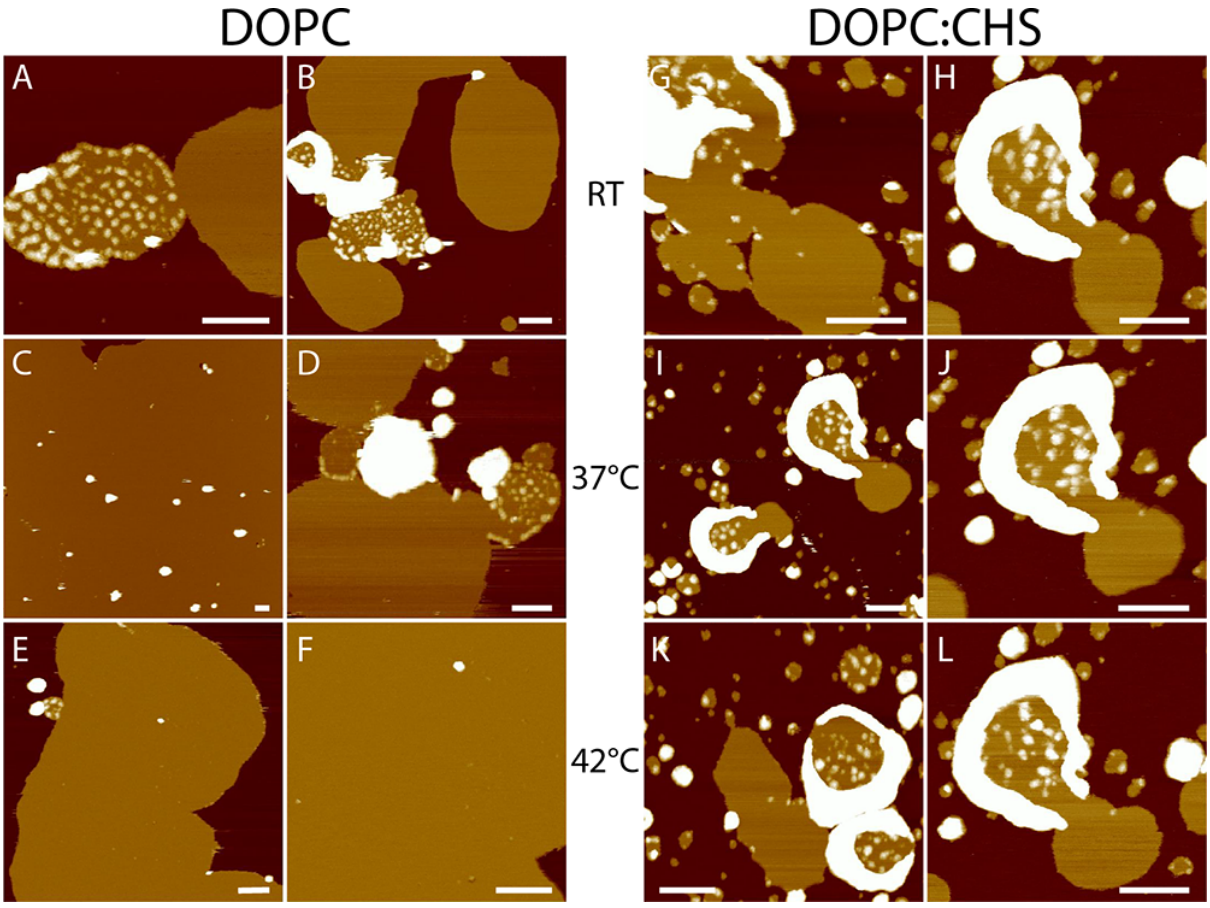

Fig. S2. AFM topographs of human β_2AR reconstituted in DOPC membranes in the presence and absence of CHS and recorded at different temperatures. (**A** to **F**) AFM topographs of β_2AR reconstituted in DOPC membranes and imaged at room temperature (25°C), 37°C, and 42°C. (**G** to **L**) AFM topographs of β_2AR reconstituted in DOPC:CHS membranes and imaged at room temperature, 37°C, and 42°C. Topographs were recorded by FD-based AFM in SMFS buffer solution (see Materials and Methods). None of the AFM topographs recorded (n > 50) revealed phase separations of the membranes made from DOPC only or made from the lipid mixture (DOPC:CHS). The white dots protruding from the membranes represent single receptors or assemblies of β_2AR. The full-range color ranges of the AFM topographs correspond to vertical scales of 20 nm (A), 19 nm (B), 32 nm (C), 28 nm (D), 20 nm (E), 19 nm (F), 17 nm (G), 18 nm (H), 17 nm (I), 18 nm (J), 19 nm (K), and 18 nm (L). Scale bars, 200 nm. Each experiment shown has been repeated at least 3 times revealing similar results.

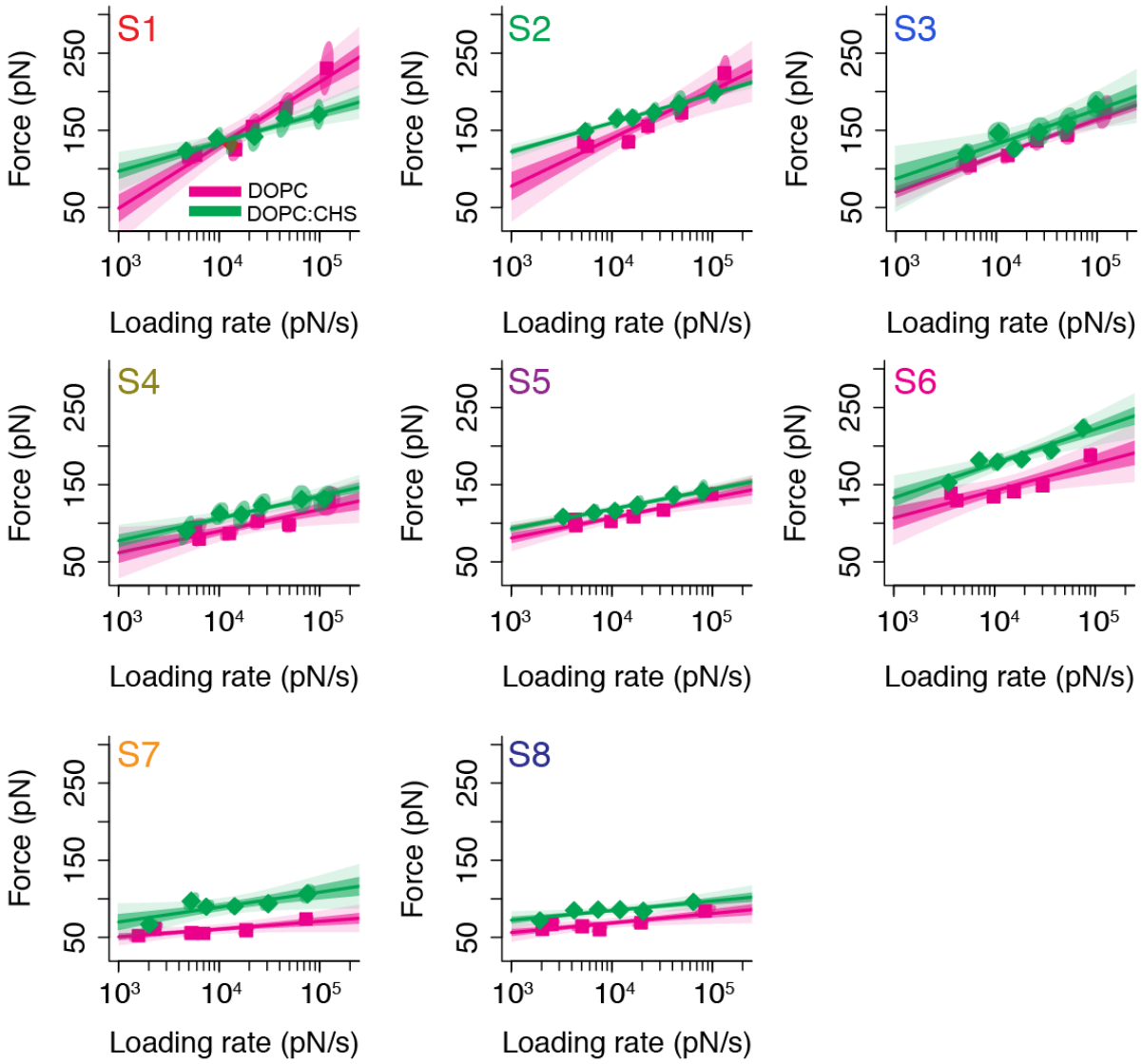

Fig. S3. CHS moderately changes the structural properties of human β_2AR at 25°C. DFS plots of each structural segment (labeled S1 to S8; Fig. 1D) stabilizing β_2AR reconstituted into phospholipid (DOPC) membranes with and without CHS at 25°C. Each DFS plot describes the dynamic behavior of a stable structural segment in the absence (pink) and presence (green) of CHS. Each data point gives the mean unfolding force versus the mean loading rate. Slanted ellipses indicate one standard error. The data points has been extracted from the force-distance curves shown in Fig. 2 (see Materials and Methods). To obtain the unfolding free-energy barrier parameters, the Bell-Evans model (*52*) was fitted (solid lines) to the DFS plots (Materials and Methods; Equation 2). Fitting confidence intervals of one (68%) and two (95%) standard deviations are indicated by dark- and light-colored regions, respectively.

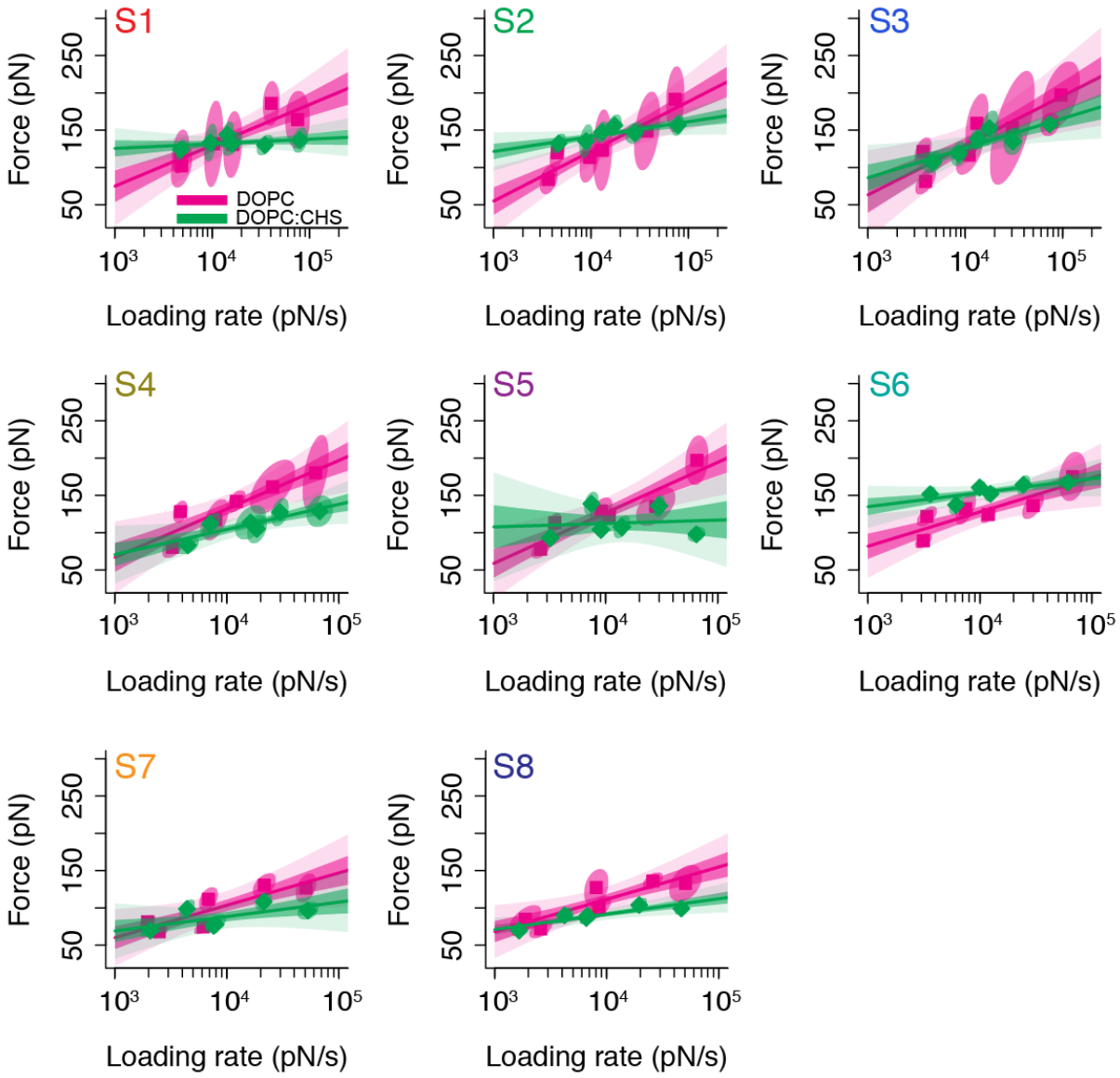

Fig. S4. CHS substantially changes the structural properties of human β_2AR at 37°C. DFS plots of each structural segment (labeled S1 to S8; Fig. 1D) stabilizing β_2AR reconstituted in phospholipid (DOPC) membranes with and without CHS at 37°C. Each DFS plot describes the dynamic behavior of a stable structural segment in the absence (pink) and presence (green) of CHS. Each data point gives the mean unfolding force versus the mean loading rate. Slanted ellipses indicate one standard error. The data points has been extracted from the force-distance curves shown in Fig. 2 (see Materials and Methods).To obtain the unfolding free-energy barrier parameters, the Bell-Evans model (*52*) was fitted (solid lines) to the DFS plots (Materials and Methods; Equation 2). Fitting confidence intervals of one (68%) and two (95%) standard deviations are indicated by dark- and light-colored regions, respectively.

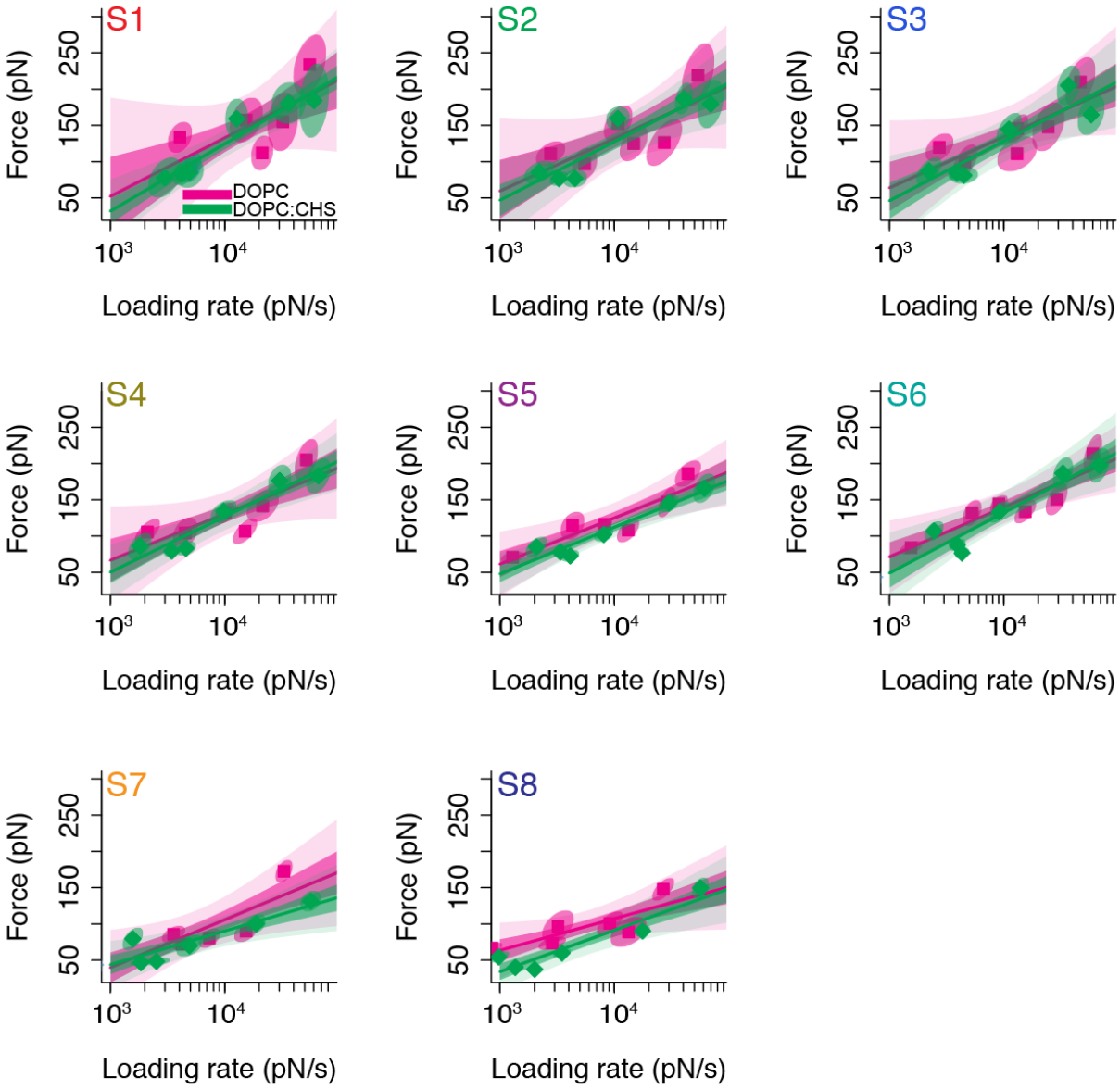

Fig. S5. CHS has little influence on the structural properties of human β_2AR at 42°C. DFS plots of each structural segment (labeled S1 to S8; Fig. 1D) stabilizing β_2AR reconstituted in phospholipid (DOPC) membranes with and without CHS at 42°C. Each DFS plot describes the dynamic behavior of a stable structural segment in the absence (pink) and presence (green) of CHS. Each data point gives the mean unfolding force versus the mean loading rate. Slanted ellipses indicate one standard error. The data points has been extracted from the force-distance curves shown in Fig. 2 (see Materials and Methods).To obtain the unfolding free-energy barrier parameters, the Bell-Evans model (*52*) was fitted (solid lines) to the DFS plots (Materials and Methods; Equation 2). Fitting confidence intervals of one (68%) and two (95%) standard deviations are indicated by dark- and light-colored regions, respectively.

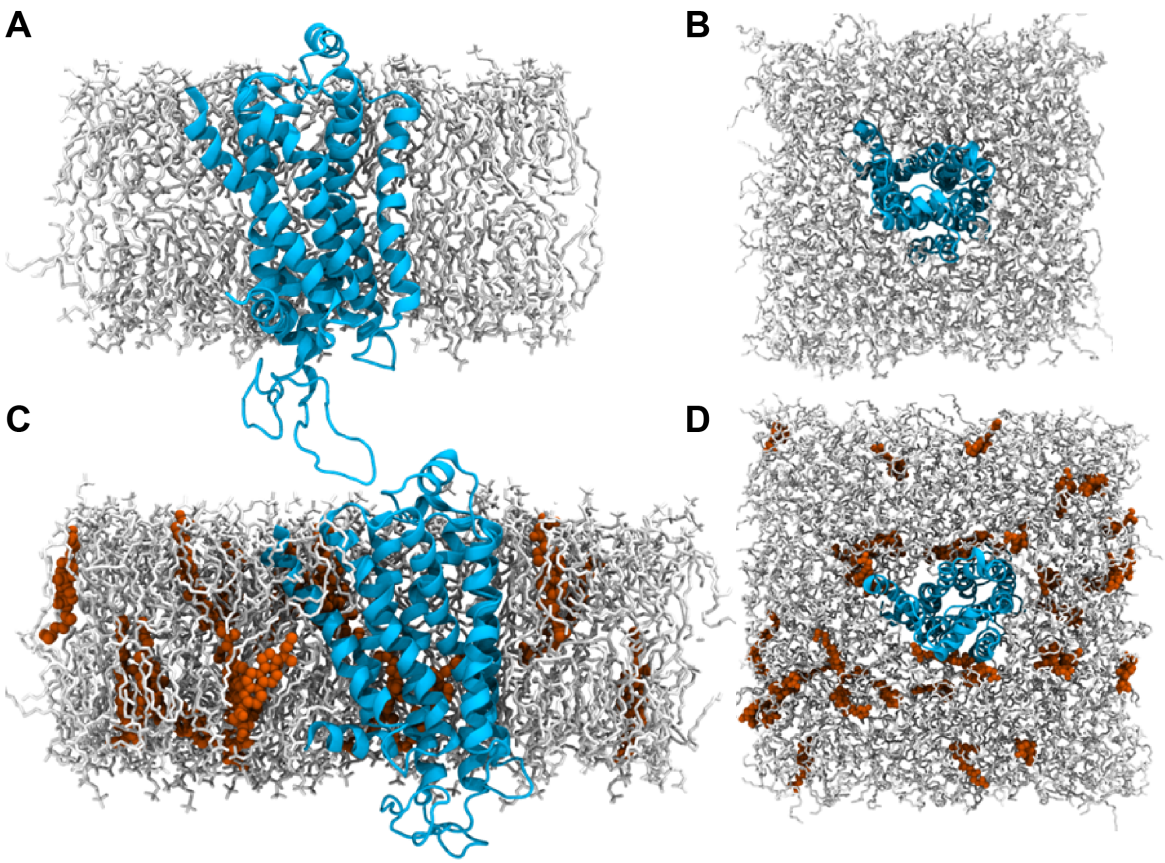

Fig. S6. Atomistic MD simulations of the β_2AR. (**A** to **D**) Side (A and C) and top (B and D) views of human β_2AR embedded in DOPC (A and B) and DOPC:CHS (C and D) membranes used in atomistic MD simulations. β_2AR is shown in cartoon form in cyan. DOPC and CHS are colored gray and orange, respectively.

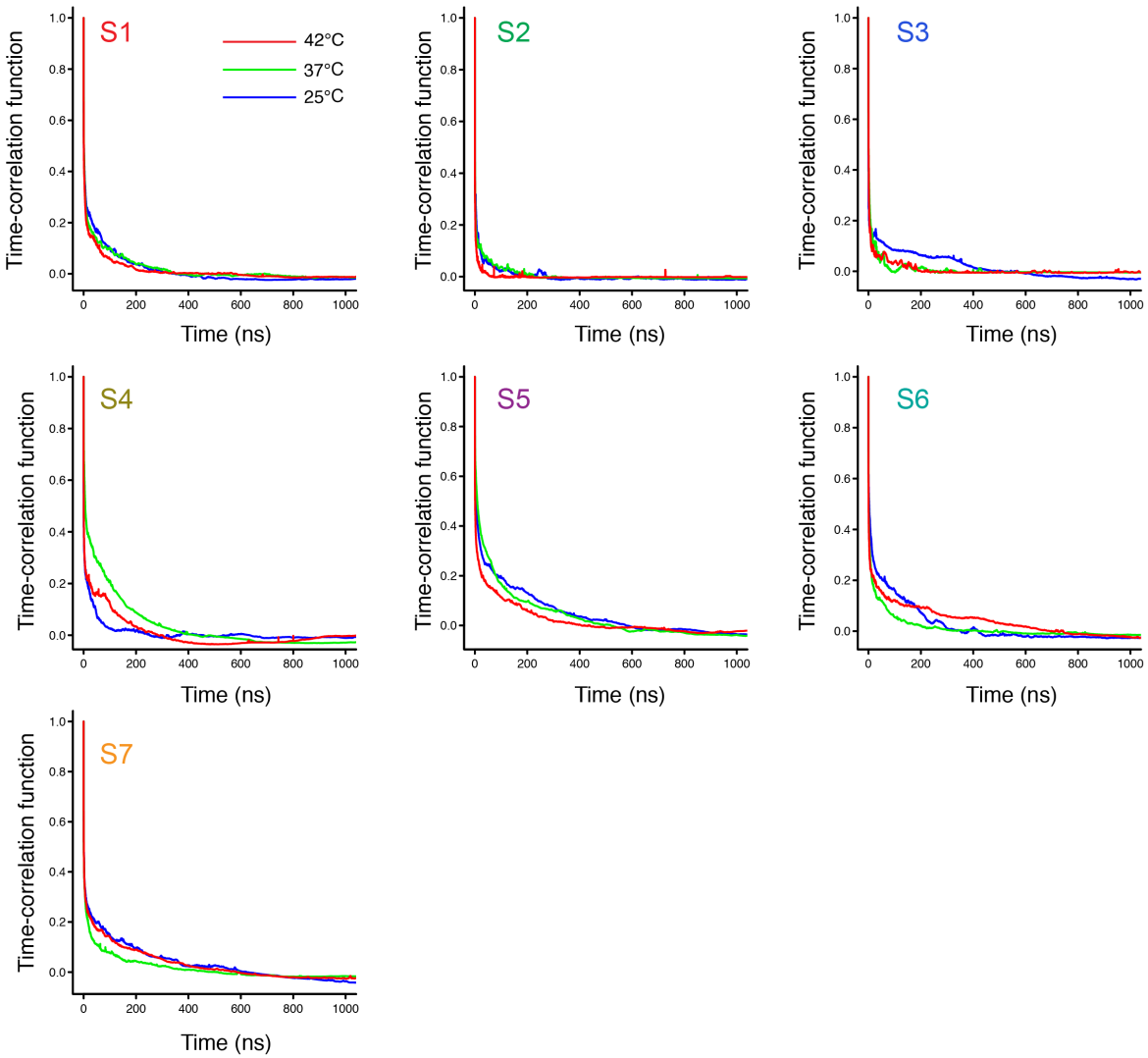

Fig. S7. Interaction times of CHS with the structural segments of β_2AR depend on the temperature. Time-correlation functions describing the interaction time of CHS with the seven structural segments (S1 to S7) of β_2AR at 25°C (blue), 37°C (green), and 42°C (red). Each condition has been simulated at least 3 independent times revealing similar results (see table S1).

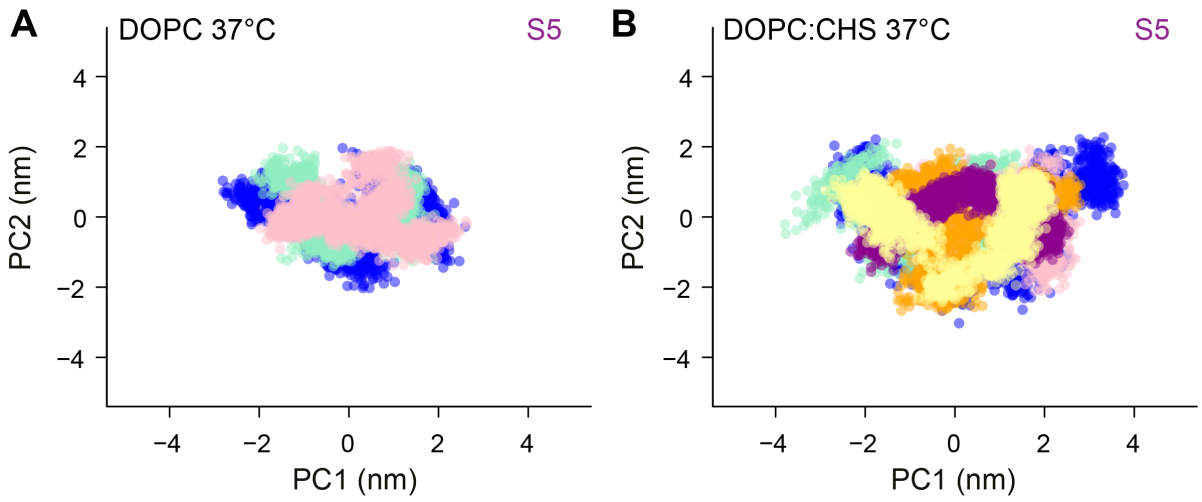

Fig. S8. Structural fluctuations of the structural segment S5 depend on the presence of CHS. (**A** and **B**) Projections of the structural fluctuations of the structural segment S5 of β_2AR in DOPC at 37°C without (A) and with (B) CHS. These projections are of simulation trajectories along the first and second principal components (PC1 and PC2). The results of three (A) and six (B) independent simulations (see table S1) are highlighted in different colors.

Table S1. Systems simulated.

System	Temperature (°C)	Number of repeats	Simulation time of each simulation repeat (μs)
β_2AR in DOPC membrane	25	3	2.5
	37	3	2.5
	42	3	2.5
β_2AR in DOPC membrane with 10 mol% CHS	25	6	2.5
	37	6	2.5
	42	6	2.5